

# Interpreting map-based $E/B$ spectral properties of CMB foregrounds

Gilles Weymann-Despres<sup>1\*</sup>, Léo Vacher<sup>2,3</sup>, Michael E. Jones<sup>1</sup>, Angela C. Taylor<sup>1</sup>, Carlo Baccigalupi<sup>2</sup>, A.J. Banday<sup>4</sup>, Richard D.P. Grumitt<sup>5</sup>, Nicoletta Krachmalnicoff<sup>2</sup>.

<sup>1</sup>*Department of Physics, University of Oxford, Denys Wilkinson Building, Keble Road, Oxford OX1 3RH, UK*

<sup>2</sup>*The International School for Advanced Studies (SISSA), via Bonomea 265, I-34136 Trieste, Italy*

<sup>3</sup>*Université Paris-Saclay, CNRS/IN2P3, IJCLab, 91405 Orsay, France*

<sup>4</sup>*IRAP, Université de Toulouse, CNRS, CNES, UPS, Toulouse, France*

<sup>5</sup>*Global College, Shanghai Jiao Tong University, Shanghai 200240, China*

Accepted XXX. Received YYY; in original form ZZZ

## ABSTRACT

Map-space  $E/B$  decompositions of linear polarization are attractive for foreground and CMB analyses because they isolate the  $B$ -family patterns that contaminate primordial tensor searches from  $E$ -family patterns that trace coherent Galactic structures. However, the  $E/B$  transform is non-fully-local and induces apparent spectral complexity in projected fields even when the underlying sky is spectrally simple in  $\underline{P} = Q + iU$ . We quantify this effect for synchrotron emission. We introduce a complex-parameter description of the frequency dependence of  $\underline{P}$ , its spin-preserving projections  $\underline{P}_E$  and  $\underline{P}_B$ , and the scalar  $\underline{S} = E + iB$ , using complex log–Taylor and moment expansions (with simple transformation rules under  $E/B$  projection) and linking their coefficients to spectral-index variations, line-of-sight mixing, synchrotron ageing, and Faraday effects. Using a toy model and a PySM template, we find that scalar combinations, especially  $|E|$  and  $|B|$ , acquire the largest induced complexity, while  $\underline{S}$  is less affected but lacks a directly interpretable amplitude and angle. By contrast,  $\underline{P}_E$  and  $\underline{P}_B$  retain a clear geometric meaning and exhibit only moderate spectral distortions, while satisfying the closure relation  $\underline{P} = \underline{P}_E + \underline{P}_B$  (which extends to all spectral orders in the moment formalism). Finally, with three frequency channels, we compare low-order spectral truncations and propose diagnostics to test whether the data favour a single power law in  $P$  or independent power laws in  $(P_E, P_B)$ . This work is intended to be of practical relevance for both Galactic science and CMB  $B$ -mode analyses and lays the conceptual foundation for a series of papers applying the framework to observational data.

**Key words:** cosmology: cosmic background radiation - ISM: magnetic fields - methods: data analysis - physical data and processes: polarization - radiation mechanisms: non-thermal - radio continuum: ISM

## 1 INTRODUCTION

Detecting the faint  $B$ -mode polarization of the Cosmic Microwave Background (CMB), a key signature of primordial gravitational waves predicted by inflation, remains a central goal in cosmology. However, this signal is obscured by polarized Galactic foregrounds, particularly synchrotron and thermal dust emission. Synchrotron radiation dominates at frequencies below a few tens of GHz and originates from cosmic ray electrons spiralling around the Galactic magnetic field (whose energy spectrum is well characterized, see, e.g., Ackermann et al. 2012). Its polarization fraction can reach up to 75% in uniform fields but is significantly reduced by magnetic field tangling, line-of-sight integration, and Faraday depolarization at low frequencies; see, e.g., Waelkens et al. (2009). Improved characterization of this polarized synchrotron foreground is essential for component separation in CMB analysis and for informing the next

generation of experiments such as the Simons Observatory (Abitbol et al. 2019) and LiteBIRD (Allys et al. 2023).

Moreover, understanding synchrotron emission is key for Galactic science. For instance, it provides valuable insight into the structure and dynamics of the Galactic magnetic field: its morphology and spectral behaviour encode information on magnetohydrodynamic turbulence, energy injection and dissipation processes in the interstellar medium that play a key role in regulating star formation across the Galaxy, see, e.g., Price et al. (2009).

At each point  $\mathbf{n}$  on the sphere, the measured quantities  $Q$  and  $U$  are the components of the symmetric, traceless spin-2 tensor  $\mathcal{P}$  (in the local orthonormal tangent basis  $(\hat{e}_\theta, \hat{e}_\phi)$ ) that describes the linear polarization state (see Hu & White 1997; Kamionkowski & Kovetz 2016). This tensor can also be expressed in terms of a polarization amplitude  $P$  and an angle  $\psi \in [-\pi/2, \pi/2]$ :

$$\mathcal{P}_{ab}(\mathbf{n}) = \frac{1}{\sqrt{2}} \begin{pmatrix} Q & U \\ U & -Q \end{pmatrix}(\mathbf{n}) = \frac{P(\mathbf{n})}{\sqrt{2}} \begin{pmatrix} \cos 2\psi & \sin 2\psi \\ \sin 2\psi & -\cos 2\psi \end{pmatrix}(\mathbf{n}). \quad (1)$$

In order to separate parity-even (radial or tangential) patterns from parity-odd (curl-like) patterns, polarization is commonly decom-

\* E-mail: gilles.weymann-despres@physics.ox.ac.uk

posed into  $E$  and  $B$  modes (Zaldarriaga & Seljak 1997; Seljak & Zaldarriaga 1997; Kamionkowski et al. 1997). Similarly, the linear polarization tensor at each point on the sphere can be viewed as a sum of two distinct terms that originate from  $E$  and  $B$  modes:

$$\mathcal{P}_{ab}(\mathbf{n}) = \mathcal{P}_{ab}^{(E)}(\mathbf{n}) + \mathcal{P}_{ab}^{(B)}(\mathbf{n}). \quad (2)$$

As shown in Appendix A, since both  $\mathcal{P}_{ab}^{(E)}$  and  $\mathcal{P}_{ab}^{(B)}$  can be expressed exclusively in spin-weighted harmonics of weight  $\pm 2$ , and since the  $E/B$  decomposition is a linear projector that commutes with rotations when acting on the harmonic coefficients of the full polarization field, each component shares the same spin-2 transformation law as  $\mathcal{P}_{ab}$ . Therefore, both  $\mathcal{P}_{ab}^{(E)}$  and  $\mathcal{P}_{ab}^{(B)}$  are themselves spin-2 tensor fields on the sphere.

Hence, analogously to  $Q$  and  $U$  in Eq. 1, we can introduce the  $E$ - and  $B$ -family Stokes parameters, defined as the components of the local-orthonormal-tangent-basis matrix representations of  $\mathcal{P}_{ab}^{(E)}$  and  $\mathcal{P}_{ab}^{(B)}$ , namely  $Q_E$ ,  $U_E$ ,  $Q_B$ , and  $U_B$ , as well as the corresponding polarization amplitudes  $P_E$ ,  $P_B$  and polarization angles  $\psi_E$  and  $\psi_B$  (see Rotti & Huffenberger 2019; Liu et al. 2018, 2023). In practice, this decomposition is especially useful for tracking, in map space, the gradient-like (irrotational) and curl-like (solenoidal) properties of the polarization through  $P_E$  and  $P_B$ , which can in general originate from distinct physical sources (see Liu 2018 or Martire et al. 2023). The more standard way to obtain  $E$ - and  $B$ -mode maps is to project its harmonic coefficients,  $a_{\ell m}^E$  and  $a_{\ell m}^B$ , as spin-0 coefficients<sup>1</sup> (see, e.g., Ade et al. 2016).

The map-space  $E/B$  separation is appealing not only as a mathematical decomposition, but also as a practical way to organize foreground information by parity. Many coherent Galactic structures (e.g. large loops and filamentary features) tend to appear predominantly in the  $E$  family, whereas their residual  $B$ -family contribution is a direct contaminant of primordial tensor perturbations. This motivates performing spectral analyses directly in  $E/B$ -separated spin-preserving fields ( $\mathcal{P}_{ab}^{(E)}$  and  $\mathcal{P}_{ab}^{(B)}$ ), rather than in  $(Q, U)$  separately (which are basis dependent) or in the total polarization  $\mathcal{P}_{ab}$  (which mixes the two parity families).

The central complication is that *map-space  $E/B$  separation is intrinsically non-fully-local*. The map-space operators that define the map-space  $E/B$  transforms act as finite-width convolutions on the sphere, so the value of an  $E/B$ -separated field at a given direction receives contributions from neighbouring structures. The corresponding real-space kernels, and their typical shapes, are shown in Appendix B. This loss of locality implies that  *$E/B$  filtering can induce additional apparent spectral complexity* in the projected fields, even when the underlying sky is spectrally simple in the total polarization  $\mathcal{P}$ .

However, for any spectral analysis, it is advantageous to work with

<sup>1</sup> **Implementation** to compute the  $E/B$ -separated fields:

The implementation of the fields introduced above is straightforward using the `healpy map2alm/alm2map` functions, see Górski et al. (2005):

$$\{I, Q, U\} \xrightarrow{\text{map2alm}} \{a_{\ell m}^I, a_{\ell m}^E, a_{\ell m}^B\}, \quad (3)$$

$$\{E, Q_E, U_E\} \xleftarrow{\text{alm2map}} \{a_{\ell m}^E, a_{\ell m}^E, 0\}, \quad (4)$$

$$\{B, Q_B, U_B\} \xleftarrow{\text{alm2map}} \{a_{\ell m}^B, 0, a_{\ell m}^B\}. \quad (5)$$

We emphasize that *these non-fully-local transforms are strictly well defined only on the full sky*. In this conceptual paper we therefore work within this simplified framework and do not address the complications arising from partial-sky analyses, which will be discussed in the next paper of the series.

fields of low spectral complexity. Such fields can be described with fewer spectral parameters, and therefore allow more robust fits when only a limited number of frequency channels are available. This is particularly important for foreground template extrapolation across frequency and for parametric component-separation methods, which must assume an explicit spectral model. Low spectral complexity is also desirable for Galactic science: if the effective spectral behaviour varies strongly across the sky and requires many degrees of freedom, then the morphology of a map is not extrapolated faithfully with frequency, and structures identified at one frequency may not have a clear counterpart at another. For these reasons, identifying field representations whose spectra remain as simple as possible is a central practical goal of this work.

In this work we detail a map-space spectral framework designed to quantify and interpret this induced complexity. We introduce complex log-Taylor and complex-moment expansions for generic complex fields, and establish the key properties that make them useful for  $E/B$ -separated analyses. In particular, we show that scalar quantities such as  $|E|$  and  $|B|$  are the most strongly affected by induced complexity, while the complex scalar  $\underline{S} = E + iB$  is less affected but does not provide a directly interpretable amplitude and angle. By contrast, the spin-2 complex fields  $\underline{P}_E$  and  $\underline{P}_B$  display only moderate (though non-negligible) induced distortions while retaining a clear geometric meaning: they satisfy the relation Eq. 2, their amplitudes and angles remain interpretable in map space, and the moment formalism promotes this relation to all spectral orders. We illustrate these points on a controlled toy model that gathers the main physical mechanisms capable of generating spectral complexity, and on a more realistic PySM synchrotron model (Thorne et al. 2017; Zonca et al. 2021; Group et al. 2025). In addition, we introduce practical three-frequency diagnostics that can be applied to data to distinguish between different effective modelling choices for the spectral behaviour of map-space  $E/B$ -separated fields.

The paper is organized as follows. In Sec. 2 we define the map-space  $E/B$ -separating complex operators and introduce the complex log-Taylor and moment parametrizations used throughout. In Sec. 3 we derive analytic predictions for the spectral signatures of several synchrotron mechanisms (spatially varying spectral index, line-of-sight mixing, intrinsic curvature, ageing, and Faraday effects). In Sec. 4 we then validate these predictions and compare the induced spectral complexity across field representations using both a toy model and a realistic PySM synchrotron sky, and we present simple diagnostics relevant for data analyses (including cases with a limited number of observed frequency channels).

## 2 $E/B$ -SEPARATING COMPLEX LINEAR OPERATORS AND SPECTRAL PROPERTIES

In this section we introduce the formalism used to describe the spectral properties of polarized emission in map space, especially when decomposed into  $E$ - and  $B$ -separated fields (before later on linking parameters to physics in Sec. 3 and testing those on toy model and PySM in Sec. 4). We first present in Sec. 2.1 the complex linear operators employed throughout this work. We then detail in Sec. 2.2 the spectral parametrizations that can be applied to the various fields. In Sec. 2.3 we examine the consequences of linearity for the  $E/B$ -projected spectral parameters. Finally, in Sec. 2.4, we summarize the conceptual advantages and limitations of the different fields.

## 2.1 $E/B$ -separating complex linear operators

For convenience, we represent the linear polarization at each sky direction by the complex spin-2 field

$$\underline{P} \equiv Q + iU, \quad (6)$$

which contains the same Stokes information as the matrix formulation of the tensor  $\mathcal{P}$ , while being simpler to manipulate and interpret. The modulus of this complex field gives the polarization amplitude  $P$ , and half of its argument gives the polarization angle  $\psi$ . In this work, any complex quantity is denoted by an underline.

A variety of linear operators can be constructed to separate  $\underline{P}$  into its  $E$ - and  $B$ -mode components.

First, we define the spin-preserving  $E/B$  projectors that implement the decomposition introduced in Eq. 2.

$$\underline{P}_E = Q_E + iU_E = \underline{L}_E[\underline{P}], \quad \underline{P}_B = Q_B + iU_B = \underline{L}_B[\underline{P}], \quad (7)$$

where  $\underline{P}_E$  and  $\underline{P}_B$  are the complex spin-2 field version of  $\mathcal{P}_{ab}^{(E)}$  and  $\mathcal{P}_{ab}^{(B)}$ , just as  $\underline{P}$  is for  $\mathcal{P}_{ab}$ . Again,  $\underline{P}_E$  and  $\underline{P}_B$  differ from  $\underline{P}$  only through the selection of  $E$ - or  $B$ -like patterns.

Second, in the more standard construction, one interprets the harmonic coefficients  $a_{\ell m}^E$  and  $a_{\ell m}^B$  as those of scalar fields, respectively called standard  $E$  and  $B$  scalar fields. We combine these into the complex scalar field

$$\underline{S} \equiv E + iB = \underline{L}_S[\underline{P}], \quad (8)$$

which contains the full information of  $\underline{P}$  but is not itself a polarization field.

On the full sphere,  $\underline{L}_E$  and  $\underline{L}_B$  have nice properties: they are *orthogonal projection operators* satisfying  $\underline{L}_X^2 = \underline{L}_X$ ,  $\underline{L}_X \underline{L}_Y = 0$  and  $\underline{L}_X + \underline{L}_Y = \mathbb{I}$  ( $X, Y \in E, B$ ), on top of being *linear*, i.e.  $\underline{L}_X(\underline{P}_1 + \lambda \underline{P}_2) = \underline{L}_X(\underline{P}_1) + \lambda \underline{L}_X(\underline{P}_2)$  for two complex polarisation fields  $\underline{P}_1$  and  $\underline{P}_2$  and a uniform scalar  $\lambda$ . Their explicit expressions, both in harmonic space and in their real-space non-fully-local forms, as well as the typical shape of their kernels, are given in Appendix B.

Eq. 2 rewritten in terms of complex spin-2 fields yields

$$\underline{P} = \underline{P}_E + \underline{P}_B, \quad (9)$$

at all frequencies. Hereafter, we refer to this as the (complex) *closure relation*. No such closure property exists for the scalar fields ( $E, B$ ).

## 2.2 Spectral parametrizations of a polarized signal

All the fields introduced so far can be observed at several different frequencies  $\nu$ , which can be used to provide a spectral description for each of them. To this end, we choose a pivot (or "reference") frequency  $\nu_0$  and define

$$s \equiv \log\left(\frac{\nu}{\nu_0}\right). \quad (10)$$

We now describe different options for modelling the spectral behaviour of a generic field, which may be real,  $X_\nu$ , or complex,  $\underline{X}_\nu$  (the dependence on  $\nu$  is hereafter denoted by a lower index). In what follows,  $\underline{X}_\nu$  may stand for any of the complex fields  $\underline{P}$ ,  $\underline{P}_E$ ,  $\underline{P}_B$ , or  $\underline{S}$ .

### 2.2.1 Real log–Taylor expansion

While the exact spectral dependence of polarized synchrotron emission is unknown and might be complex (as we will emphasize later on), one expects it not to deviate strongly from a power law, see, e.g., Pacholczyk (1970).

A commonly used way to parametrize the frequency dependence of a quasi-power-law real-valued SED is to expand the logarithm of the field, see for instance Rybicki (2004) in the context of synchrotron emission, yielding a "tilt" and "curvature":

$$X_\nu = A \exp\left(\beta s + \frac{1}{2}\gamma s^2 + \dots\right), \quad (11)$$

where  $A$  is an amplitude,  $\beta$  is a spectral tilt, and  $\gamma$  is a curvature parameter. If applied to the polarization amplitude  $P$ , e.g. Akrami et al. (2020); Galloway et al. (2023); Adak et al. (2025); Rizzieri et al. (2025), this parametrization implicitly assumes a polarization angle that is constant with frequency, which need not hold in general.

One might instead apply this expansion to  $Q$  and  $U$  (see de la Hoz et al. 2023 for a comparison with  $P$  in a practical case), or even to  $E$  and  $B$  individually. Although this is straightforward numerically, it is conceptually unsatisfactory for at least two reasons: (i) the expansion does not allow for a sign change in  $X_\nu$ , which frequently occurs for non-positive-definite fields such as  $Q$ ,  $U$ ,  $E$ , or  $B$ ; and (ii) the two fields should vary coherently according to the underlying polarization angle  $\psi$ , reflecting the geometrical relationship that unifies them.

### 2.2.2 Complex log–Taylor expansion

To overcome the limitations of a real log–Taylor expansion, it is natural to consider directly the spectral behaviour of the *complex* field  $\underline{X}_\nu$  itself. As already emphasized in Sec. 2.1, this choice follows from the fact that the linear polarization field is fundamentally a spin-2 object, whose physically meaningful degrees of freedom are not the real components ( $Q, U$ ) taken separately, but their joint amplitude and orientation in the complex plane. Treating  $Q$  and  $U$  as independent real fields implicitly breaks this geometric structure and makes it difficult to describe coherent frequency evolution of the polarization angle, sign changes, or rotations in a robust and coordinate-independent manner.

By contrast, working with complex fields preserves the intrinsic geometry of the polarization maps and allows amplitude and angle variations to be encoded simultaneously and consistently. In particular, a complex spectral expansion provides a minimal and well-defined way to capture both changes in polarization intensity and frequency-dependent rotations of the polarization direction within a single set of parameters. Although such complex parametrizations have been implicitly used in specific contexts, their systematic application to map-space spectral modelling of polarized foregrounds is not standard, and constitutes a central ingredient of the present work.

Hence, we introduce the "complexified" version of the log–Taylor expansion, which reads

$$\underline{X}_\nu = \underline{A} \exp\left(\underline{\beta} s + \frac{1}{2}\underline{\gamma} s^2 + \dots\right), \quad (12)$$

where  $\underline{A}$  is a complex amplitude,  $\underline{\beta}$  a complex spectral tilt, and  $\underline{\gamma}$  a complex curvature. Denoting by  $\underline{\kappa}_n$  the  $n$ -th log–Taylor spectral parameter ( $\underline{\kappa}_0 = \log \underline{A}$ ,  $\underline{\kappa}_1 = \underline{\beta}$ ,  $\underline{\kappa}_2 = \underline{\gamma}$ ), we can obtain it as

$$\underline{\kappa}_n = \frac{d^n}{ds^n} \log \underline{X}_\nu \Big|_{\nu_0}. \quad (13)$$

Under the restrictive (and somewhat unrealistic) assumption that the polarization angle is strictly constant with frequency, the real log–Taylor coefficients can be identified with the real parts of the complex ones. When the polarization angle  $\psi$  varies with frequency, the imaginary parts of the log–Taylor parameters are directly related

to the successive derivatives of  $\psi$ :

$$\begin{cases} \log A = \Re(\log \underline{A}) = \log |\underline{A}|, \\ \beta = \Re(\underline{\beta}), \\ \gamma = \Re(\underline{\gamma}), \end{cases} \quad \text{and} \quad \begin{cases} \psi = \frac{1}{2} \Im(\log \underline{A}), \\ \frac{d\psi}{ds} = \frac{1}{2} \Im(\underline{\beta}), \\ \frac{d^2\psi}{ds^2} = \frac{1}{2} \Im(\underline{\gamma}). \end{cases} \quad (14)$$

### 2.2.3 Complex moment expansion

Working with complex log-Taylor parameters for low-frequency polarized emission is a novel viewpoint and, as we emphasize below, it can be closely linked to the underlying physics. A related complex formalism has previously been proposed through the spin-moment expansion (Vacher et al. 2023a,b), which generalizes the original moment expansion proposed by Chluba et al. (2017) to polarized signals using complex numbers. This formalism has also been applied to foreground modelling (Vacher et al. 2025) and to study the emission properties of thermal dust with the Planck-HFI data (Guillet et al. 2025). More generally, moment expansion has been largely applied by the CMB community in various forms and spaces (pixels, needlets and power-spectra) in order to perform component separation for recent ground- and space-based missions (see, e.g., Ichiki et al. 2019; Azzoni et al. 2021; Mangilli et al. 2021; Vacher et al. 2022; Remazeilles et al. 2021; Azzoni et al. 2023; Wolz et al. 2024; Carones & Remazeilles 2024; Liu et al. 2025).

The spin-moment expansion of a complex field  $\underline{X}_\nu$  requires expanding around a reference power law:

$$\underline{X}_\nu = \left(\frac{\nu}{\nu_0}\right)^{\bar{\beta}} \left(w_0 + w_1 s + \frac{w_2}{2} s^2 + \dots\right), \quad (15)$$

where  $\bar{\beta}$  is a fixed, real reference spectral index chosen to represent a typical mean-sky value, and  $w_n$  is the complex moment of order  $n$ . These moments can be obtained from

$$w_n = \frac{d^n}{ds^n} \left[ \underline{X}_\nu \exp(-\bar{\beta}s) \right] \Big|_{\nu_0}. \quad (16)$$

This expansion was first introduced in order to model the astrophysical signal resulting from the averaging of non-linear SEDs, and we will argue here that its range of application is much broader. We return to the corresponding physical predictions for the moments in Sec. 3.

Another option would be to choose a pixel-dependent reference index  $\bar{\beta}(\mathbf{n})$ . We do not adopt this choice, because it breaks the full-sky linearity of Eq. 15. Linearity is especially useful in the present work, as it allows all linear operators to commute trivially with the expansion. If  $\bar{\beta}$  were allowed to vary across the sky, several expressions derived below would be altered<sup>2</sup>.

### 2.2.4 Relations between complex log-Taylor parameters and moments

Expanding Eqs. 13 and 15 around  $s = 0$ , equating the two representations, matching orders, and solving for the log-Taylor parameters

<sup>2</sup> For example, the compensating term involving  $w_1$  in the last line of Eq. 17 arises exactly because the expansion uses a *fixed* reference  $\bar{\beta}$ . A spatially varying reference index would absorb this term, yielding the simpler relation  $\gamma = w_2/w_0$ .

yields

$$\begin{cases} \underline{A} = w_0, \\ \underline{\beta} = \bar{\beta} + \frac{w_1}{w_0}, \\ \underline{\gamma} = \frac{w_2}{w_0} - \left(\frac{w_1}{w_0}\right)^2. \end{cases} \quad (17)$$

Inverting these relations, we obtain for the moments

$$\begin{cases} w_0 = \underline{A}, \\ w_1 = \underline{A} (\underline{\beta} - \bar{\beta}), \\ w_2 = \underline{A} \left[ (\underline{\beta} - \bar{\beta})^2 + \underline{\gamma} \right]. \end{cases} \quad (18)$$

Thus, the moment expansion and the log-Taylor expansion provide mathematically equivalent, but conceptually distinct, spectral descriptions of a complex field. Furthermore, a curvature in the log-Taylor expansion can be reabsorbed as a second order moment, an observation already made in Remazeilles et al. (2021).

For both parametrizations, the real and imaginary parts of the spectral parameters can be related to the frequency evolution of the amplitude and angle of the corresponding complex field. To first order in  $s$ , the log-amplitude and the angle of  $\underline{X}_\nu$  can be expressed as

$$\log |\underline{X}_\nu| \simeq \log A + \Re(\underline{\beta}) s \simeq \log |w_0| + \bar{\beta} s + \Re\left(\frac{w_1}{w_0}\right) s, \quad (19)$$

$$\psi_\nu \simeq \psi_{\nu_0} + \frac{1}{2} \Im(\underline{\beta}) s \simeq \psi_{\nu_0} + \frac{1}{2} \Im\left(\frac{w_1}{w_0}\right) s, \quad (20)$$

consistently with Eq. 22 of Vacher et al. (2023b). Equation 20 shows that, at first order, the stability of the polarization angle across frequency is directly encoded in the imaginary part of  $w_1/w_0$ .

## 2.3 Consequences of linearity for the *E/B*-projected spectral parameters

Because  $\underline{L}_E$ ,  $\underline{L}_B$ , and  $\underline{L}_S$  are linear operators acting on complex fields, they commute with the formation of linear combinations in the moment expansion. Therefore, for all  $n \geq 0$ ,

$$\underline{w}_{n,E} = \underline{L}_E[w_n], \quad \underline{w}_{n,B} = \underline{L}_B[w_n], \quad \underline{w}_{n,S} = \underline{L}_S[w_n]. \quad (21)$$

Thanks to these simple relations, all the formalism introduced so far can be directly translated to the  $\underline{P}_E$  and  $\underline{P}_B$  fields. For instance, Eq. 20 simply applies to  $\underline{P}_E$  and  $\underline{P}_B$ , and the imaginary part of these relationships tells how the complex spin-2 *E/B* fields turn in the complex plane with frequency. Another important consequence is that the closure relation at each frequency also applies to *E* and *B* decomposed complex moments:

$$\underline{w}_n = \underline{w}_{n,E} + \underline{w}_{n,B}. \quad (22)$$

This leads to more detailed relations for the Taylor spectral parameters, which can be derived straightforwardly using Eq. 17. The log-Taylor parameters for  $\underline{P}$  can be expressed as a function of those

of  $\underline{P}_E$  and  $\underline{P}_B$ :

$$\begin{cases} P = |\underline{A}_E + \underline{A}_B| = \sqrt{P_E^2 + P_B^2 + 2P_E P_B \cos[2(\psi_E - \psi_B)]}, \\ \psi = \frac{1}{2} \arg(\underline{A}_E + \underline{A}_B) = \frac{1}{2} \arctan\left(\frac{P_E \sin 2\psi_E + P_B \sin 2\psi_B}{P_E \cos 2\psi_E + P_B \cos 2\psi_B}\right), \\ \beta = \Re\left[\frac{\underline{A}_E \beta_E + \underline{A}_B \beta_B}{\underline{A}_E + \underline{A}_B}\right], \\ \frac{d\psi}{ds} = \frac{1}{2} \Im\left[\frac{\underline{A}_E \beta_E + \underline{A}_B \beta_B}{\underline{A}_E + \underline{A}_B}\right], \\ \gamma = \Re\left[\frac{\underline{A}_E(\beta_E^2 + \gamma_E) + \underline{A}_B(\beta_B^2 + \gamma_B)}{\underline{A}_E + \underline{A}_B} - \beta^2\right], \\ \frac{d^2\psi}{ds^2} = \frac{1}{2} \Im\left[\frac{\underline{A}_E(\beta_E^2 + \gamma_E) + \underline{A}_B(\beta_B^2 + \gamma_B)}{\underline{A}_E + \underline{A}_B} - \beta^2\right]. \end{cases} \quad (23)$$

Developing moduli and arguments in these relations quickly leads to cumbersome expressions. Above, we have only displayed the explicit results for the polarization amplitude and angle, which remain tractable and we consistently recover, for the polarization angle, Eq. 3.2 of Liu et al. (2018). An important consequence of the amplitude relation is that  $(P_E - P_B)^2 < P^2 < (P_E + P_B)^2$ , restricting the  $(P_E/P, P_B/P)$  plane to

$$\begin{cases} P_B/P < P_E/P + 1, \\ P_B/P > P_E/P - 1, \\ P_B/P > -P_E/P + 1. \end{cases} \quad (24)$$

Once again, no analogous identity exists for  $(E, B)$  or for  $\underline{S}$ . Even though spectral expansions can be inferred in  $(E, B, \underline{S})$ , only the spin-preserving maps retain spectral parameters that can be interpreted directly in terms of the frequency dependence of polarization amplitudes and angles.

#### 2.4 Conceptual advantages of the $\underline{P}_E$ and $\underline{P}_B$ decomposition

The spin-preserving fields  $\underline{P}_E$  and  $\underline{P}_B$  enjoy several conceptual advantages over the scalar fields  $(E, B)$  or the complex scalar  $\underline{S} = E + iB$ . By construction they retain the geometric nature of the underlying polarization field: they remain spin-2 quantities with amplitudes and polarization angles that may (with due caution) be interpreted locally in map space. Although the meaning of these angles requires care (they are the angles after  $E/B$  filtering, not necessarily those of the underlying emission components) their interpretation remains considerably more direct than that of scalar fields obtained through the spin-2  $\rightarrow$  spin-0 conversion.

One could be worried that  $\underline{P}_E$  and  $\underline{P}_B$  are somewhat ‘‘coordinate dependent’’ whereas  $E$  and  $B$  are not. However, this is simply entirely analogous to the familiar distinction between the spin-2 field  $\underline{P} = Q + iU$  and the scalar temperature  $T$ :  $\underline{P}_E$  and  $\underline{P}_B$  are spin-2 fields that transform with a phase under local rotations of the polarization basis, while  $E$  and  $B$  are scalar, basis-invariant quantities built from them. While the coordinates of these spin-2 objects in a specific basis are obviously not basis independent,  $\underline{P}_E$  and  $\underline{P}_B$  taken as proper spin-2 objects are just as coordinate independent as  $\underline{P}$ ,  $E$ ,  $B$  or  $T$  are.

A further advantage is the closure relation, which holds identically at all frequencies and at every order in any spectral expansion. This allows a direct, term-by-term comparison between the full field and its gradient- and curl-like contributions. In particular, differences between the moments of  $\underline{P}$ ,  $\underline{P}_E$ , and  $\underline{P}_B$  admit an immediate phys-

ical interpretation in terms of the relative spectral behaviour of the corresponding spatial patterns.

A familiar diagnostic in map space is the ratio of amplitudes  $|\underline{P}_E|/|\underline{P}_B|$ , which quantifies, along each line of sight, the balance between the  $E$ -like and  $B$ -like contributions to the total polarization pattern. The moment expansion naturally generalizes this idea to any spectral order. Ratios such as  $|w_{n,E}|/|w_{n,B}|$  provide direction- and order-dependent measures of how the  $E/B$  balance varies across frequency. For example, a relative increase of  $|w_{1,B}|$  compared to  $|w_{1,E}|$  immediately indicates that curl-like structures respond more strongly to spectral-index variations than gradient-like ones. Higher-order ratios  $|w_{n,E}|/|w_{n,B}|$  (for  $n \geq 2$ ) in turn probe the curvature of this behaviour, distinguishing between frequency-dependent morphological changes driven by coherent structures, turbulence, or Faraday effects. These quantities have simple interpretations only when the fields remain spin-2, which is no longer the case for  $(E, B)$  or for the scalar  $\underline{S}$ .

By contrast, although the scalar field  $\underline{S} = E + iB$  contains the same information as  $\underline{P}$ , the interpretation of its spectral parameters is less direct: its amplitude and phase are not related to observable polarization angles or magnitudes, but to scalar quantities whose connection to the underlying geometry of the magnetic fields is non-fully-local. For this reason, moments such as  $w_{n,S}$  lack the intuitive map-space meaning of their spin-2 counterparts.

For all these reasons, the decomposition into  $\underline{P}_E$  and  $\underline{P}_B$  provides, from a conceptual standpoint, a particularly natural framework for studying the frequency dependence of the polarization field. We will illustrate this in more detail with concrete examples in Sec. 4.

### 3 PHYSICAL MECHANISMS GENERATING SYNCHROTRON SPECTRAL MOMENTS

In this section we summarize the main physical mechanisms that generate non-zero spectral moments  $w_n$  of the complex polarization field  $\underline{P}$  and of its spin-preserving projections  $\underline{P}_E$  and  $\underline{P}_B$ . Specifically, after deriving useful equations for the multiplicative corrections to an underlying spectrum in Sec. 3.1, we discuss five families of mechanisms that produce non-zero higher-order spectral parameters:

- (i) line-of-sight superposition of components with distinct power-law spectra (see Sec. 3.2);
- (ii) spatially varying spectral indices  $\beta(\mathbf{n})$  for a single emitting component per line of sight (see Sec. 3.3);
- (iii) line-of-sight superposition of components with distinct curved spectra (see Sec. 3.4);
- (iv) synchrotron ageing, which produces a smooth spectral break (see Sec. 3.5);
- (v) Faraday rotation and depolarization, which introduce both amplitude and phase effects (see Sec. 3.6).

We focus on the essential formulae and their physical interpretation, and refer the reader to the cited literature for detailed derivations. We conclude in Sec. 3.7 with a brief discussion of the coexistence of  $E$ - and  $B$ -dominated structures and the impact of the non-full-locality of the  $E/B$  operators.

#### 3.1 General considerations

To organize the predictions for spectral parameters, we express departures from a reference power law as multiplicative corrections.

For a generic complex field  $\underline{X}_\nu$  we write

$$\underline{X}_\nu = \underline{X}_0 \left( \frac{\nu}{\nu_0} \right)^{\bar{\beta}} \underline{C}(\nu), \quad (25)$$

$$= \sum_i \underline{X}_{i,0} \left( \frac{\nu}{\nu_0} \right)^{\beta_i} \prod_k \underline{C}_k^{(i)}(\nu). \quad (26)$$

where  $\underline{C}$  is a map-space frequency-dependent correction field such that  $\underline{C}(\nu_0) = 1$  by construction, and in general, which can be described in terms of several emitting components  $i$  present along the line of sight, each affected by several multiplicative physical effects  $k$ , denoted  $\underline{C}_k^{(i)}(\nu)$ . In terms of  $s$  (introduced in Eq. 10), this becomes  $\underline{X}_\nu = \underline{X}_0 \exp(\bar{\beta}s) \underline{C}(s)$ .

The complex log–Taylor parameters of  $\underline{X}_\nu$  can then be written as

$$\kappa_n = \frac{d^n}{ds^n} \left[ \log \underline{X}_\nu \right] \Big|_{s=0} = \frac{d^n}{ds^n} \left[ \log \underline{X}_{\nu_0} + \bar{\beta}s + \log \underline{C}(s) \right] \Big|_{s=0}. \quad (27)$$

In the specific case of a single emitting component present along the line of sight affected by several multiplicative physical effects  $k$ , the three first log–Taylor parameters read

$$\underline{A} = \underline{X}_0, \quad (28)$$

$$\underline{\beta} = \bar{\beta} + \sum_k \frac{d}{ds} \log \underline{C}_k(s) \Big|_0, \quad (29)$$

$$\kappa_n = \sum_k \kappa_{k,n} = \sum_k \frac{d^n}{ds^n} \log \underline{C}_k(s) \Big|_0, \quad n \geq 2. \quad (30)$$

Moreover, in the general case, the formula for the complex moments follow from Eq. 16 as

$$\underline{w}_n = \frac{d^n}{ds^n} \left[ \underline{X}_\nu e^{-\bar{\beta}s} \right] \Big|_{s=0} = \underline{w}_0 \frac{d^n}{ds^n} \underline{C}(s) \Big|_{s=0}, \quad (31)$$

In the case of several emitting components  $i$  present along the line of sight, each affected by several multiplicative physical effects  $k$ , the first three complex moments read

$$\underline{w}_0 = \sum_i \underline{X}_{i,0}, \quad (32)$$

$$\underline{w}_1 = \sum_i \underline{X}_{i,0} \frac{d \log \underline{C}^{(i)}}{ds} \Big|_0 = \sum_i \underline{X}_{i,0} \left[ (\beta_i - \bar{\beta}) + \sum_k \frac{d \log \underline{C}_k^{(i)}}{ds} \Big|_0 \right], \quad (33)$$

$$\begin{aligned} \underline{w}_2 &= \sum_i \underline{X}_{i,0} \left[ \frac{d \log \underline{C}^{(i)}}{ds} \Big|_0^2 + \frac{d^2 \log \underline{C}^{(i)}}{ds^2} \Big|_0 \right] \\ &= \sum_i \underline{X}_{i,0} \left\{ \left[ (\beta_i - \bar{\beta}) + \sum_k \frac{d \log \underline{C}_k^{(i)}}{ds} \Big|_0 \right]^2 + \sum_k \frac{d^2 \log \underline{C}_k^{(i)}}{ds^2} \Big|_0 \right\}. \end{aligned} \quad (34)$$

with  $\underline{w}_0 = \underline{X}_0$  since  $\underline{C}_0 = 1$ .

As a trivial illustration, consider  $N$  emitting components on the line of sight, all sharing the same spectral index  $\beta_i = \bar{\beta}$  and no additional effects. Then

$$\underline{P}_\nu = \sum_{i=1}^N \underline{P}_{i,0} \left( \frac{\nu}{\nu_0} \right)^{\bar{\beta}} = \underline{P}_0 \left( \frac{\nu}{\nu_0} \right)^{\bar{\beta}} \underline{C}_{\bar{\beta}}, \quad (35)$$

$$\underline{C}_{\bar{\beta}} = \sum_{i=1}^N \frac{\underline{P}_{i,0}}{\underline{P}_0}, \quad (36)$$

which is independent of frequency. In this case, the equations above trivially imply that all higher-order spectral moments vanish,  $\underline{w}_n = 0$  for  $n \geq 1$ , and the log–Taylor parameters have  $\kappa_n = 0$  for  $n \geq 2$ .

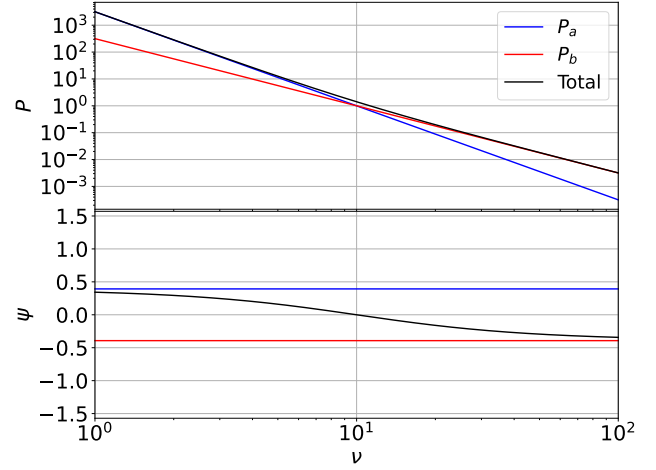


**Figure 1.** Example of the power law superposition effect (Sec. 3.2): Eq. 37 with two components,  $\underline{P}_\nu = \underline{P}_{a,\nu} + \underline{P}_{b,\nu}$  with  $\underline{P}_{a,0} = e^{2i\pi/8}$ ,  $\beta_a = -3.5$ ,  $\underline{P}_{b,0} = e^{-2i\pi/8}$  and  $\beta_b = -2.5$ . Upper panel: SED, lower panel: polarization angle, both as functions of frequency. The blue curves describe the baseline polarization spectrum, which is modified into the total black curves by the superimposition effect (whose correction  $\underline{C}_{\text{LoS}}(\nu)$  is shown in dashed-red).

### 3.2 Line-of-sight superposition of distinct power laws

We now consider multiple components along the line-of-sight (LoS hereafter) with different spectral indices:

$$\underline{P}_\nu = \sum_{i=1}^N \underline{P}_{i,0} \left( \frac{\nu}{\nu_0} \right)^{\beta_i} = \underline{P}_0 \left( \frac{\nu}{\nu_0} \right)^{\bar{\beta}} \underline{C}_{\text{LoS}}(\nu), \quad \text{where}$$

$$\underline{C}_{\text{LoS}}(\nu) = \sum_{i=1}^N \frac{\underline{P}_{i,0}}{\underline{P}_0} \left( \frac{\nu}{\nu_0} \right)^{\beta_i - \bar{\beta}}. \quad (37)$$

Substituting  $\underline{C}_{\text{LoS}}$  into Eq. 31 yields (see also Vacher et al. 2023b)

$$\underline{w}_n = \sum_i \underline{P}_{i,0} (\beta_i - \bar{\beta})^n. \quad (38)$$

Because the sum of power laws is not itself a power law in general, higher-order log–Taylor terms are generated. Using either Eq. 27 or Eq. 17, and defining complex weighted averages

$$\langle \underline{X}_i \rangle \equiv \frac{\sum_i \underline{P}_{i,0} \underline{X}_i}{\sum_j \underline{P}_{j,0}}, \quad (39)$$

one finds

$$\underline{\beta} = \langle \underline{\beta}_i \rangle, \quad (40)$$

$$\underline{\gamma} = \langle \underline{\beta}_i^2 \rangle - \langle \underline{\beta}_i \rangle^2, \quad (41)$$

and similarly for higher orders. Hence, superposition of power laws induces curvature that is equal to the complex-weighted variance of the spectral indices of the complex power laws along the LoS. In general, for arbitrary amplitudes and angles  $\underline{P}_{i,0}$ , these coefficients are complex. The imaginary parts encode a frequency-dependent polarization angle. Using Eq. 20, the first-order angle evolution around  $s = 0$  is

$$\psi_\nu \approx \psi_{\nu_0} + \frac{1}{2} \Im \left( \frac{\sum_i \underline{P}_{i,0} (\beta_i - \bar{\beta})}{\sum_i \underline{P}_{i,0}} \right) s. \quad (42)$$

This frequency-dependent angle induces intrinsic  $E \leftrightarrow B$  mixing. At zeroth order, the  $E/B$  ratio is that of the total field  $\underline{P}_0 = \sum_i \underline{P}_{i,0}$ .

At higher order however,

$$\frac{|w_{n,E}|}{|w_{n,B}|} = \frac{\left| \sum_i P_{i,E,0} (\beta_i - \bar{\beta})^n \right|}{\left| \sum_i P_{i,B,0} (\beta_i - \bar{\beta})^n \right|} \quad (43)$$

characterizes the frequency-dependent redistribution between  $E$ -like and  $B$ -like structures. There is no simpler generic expression unless we know the whole map. A non-zero imaginary part of  $w_1$  drives a change in the  $E/B$  balance with frequency, so that  $|w_{1,E}|/|w_{1,B}|$  can differ significantly from  $|P_{0,E}|/|P_{0,B}|$ .

One can also assess the relative stability of the polarization angle for different fields, *e.g.*, by comparing  $\Im(w_{1,E}/w_{0,E})$  with  $\Im(w_1/w_0)$  as a measure of how strongly  $P_E$  and  $P$  respond to line-of-sight mixing.

We display in Fig. 1 the effect of superposing two components along the line of sight with different  $\beta$  and  $\psi$ . The SED amplitude (*upper panel*) is affected by higher-order complexity around the pivot scale, and the polarization angle evolves from  $\psi_a$  at low frequency to  $\psi_b$  at high frequency (*lower panel*) (as for the next examples of this section, the absolute values and units of polarization do not matter for the discussion).

### 3.3 Spatially varying $\beta$ (single component per LoS)

Spatial variations of the synchrotron spectral index  $\beta(\mathbf{n})$  induce a direction-dependent deviation from the reference index  $\bar{\beta}$ . For a single component per pixel,

$$P_\nu = P_0 \left( \frac{\nu}{\nu_0} \right)^\beta = P_0 \left( \frac{\nu}{\nu_0} \right)^{\bar{\beta}} C_\beta(\nu), \quad \text{where } C_\beta(\nu) = \left( \frac{\nu}{\nu_0} \right)^{\beta - \bar{\beta}}. \quad (44)$$

Using Eq. 31, one obtains the hierarchy (see, *e.g.*, Vacher et al. 2023b)

$$w_n = P_0 (\beta - \bar{\beta})^n, \quad (45)$$

which is the  $N = 1$  case of Eq. 38 above. Because the spectrum in each pixel remains a pure power law, the log–Taylor curvature  $\gamma$  and all higher-order log–Taylor parameters vanish locally:  $\kappa_n = 0$  for  $n \geq 2$ , and  $w_n/w_0$  is purely real. At the level of  $P$  itself there is therefore no intrinsic curvature and no frequency evolution of the local polarization angle.

For the  $E/B$  decomposition, however, the situation is more subtle because  $L_E$  and  $L_B$  are non-fully-local operators on the sphere. On a discrete sky, let pixel indices  $p$  and  $q$  correspond to line-of-sight directions  $\mathbf{n}$  and  $\mathbf{n}'$ , respectively. In Appendix B we give the map-space expressions of the convolution kernels that implement  $L_E$  and  $L_B$ . Using Eq. B7 and B8 and substituting the spatially varying power law  $P_{\nu,q} = P_{0,q} (\nu/\nu_0)^{\beta(q)}$  yields

$$P_{E,\nu,p} = \sum_q \left[ \mathcal{K}_{E,pq}^{(+)} P_{0,q} + \mathcal{K}_{E,pq}^{(-)} P_{0,q}^* \right] \left( \frac{\nu}{\nu_0} \right)^{\beta(q)}, \quad (46)$$

$$P_{B,\nu,p} = \sum_q \left[ \mathcal{K}_{B,pq}^{(+)} P_{0,q} + \mathcal{K}_{B,pq}^{(-)} P_{0,q}^* \right] \left( \frac{\nu}{\nu_0} \right)^{\beta(q)}, \quad (47)$$

where the kernels  $\mathcal{K}_{E/B,pq}^{(\pm)}$  are frequency-independent and depend only on geometry (Euler angles between  $\mathbf{n}$  and  $\mathbf{n}'$ ) and on the radial functions  $\mathcal{K}_E, \mathcal{K}_B$  from Rotti & Huffenberger (2019) (see Appendix B). Eq. 47 shows that, for a fixed pixel  $p$  in  $P_E$  or  $P_B$ , the spectrum is a weighted superposition of power laws with different indices  $\beta(q)$ , in complete analogy with line-of-sight mixing, see Sec. 3.2.

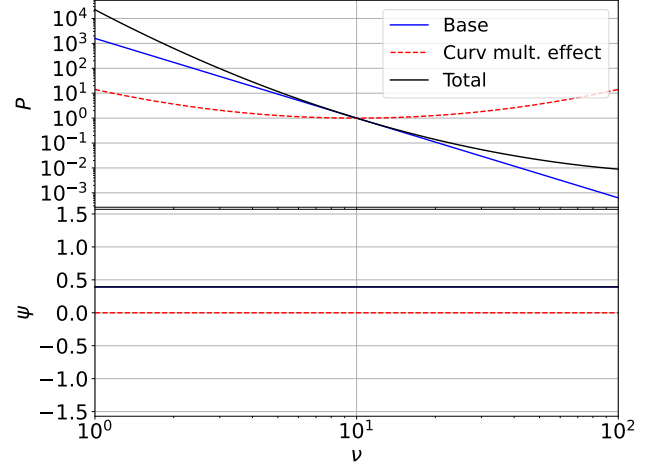


**Figure 2.** Example of a single-component intrinsic positive curvature effect (Sec. 3.4): Eq. 48 with  $P_0 = e^{2i\pi/8}$ ,  $\bar{\beta} = -3.2$  and  $\gamma = 1$ . The panels and curves are otherwise similar to the ones in Fig. 1.

Formally one still has the projected moments Eq. 21 but since  $w_n(q) \propto P_{0,q} (\beta(q) - \bar{\beta})^n$  contains a spatially varying scalar factor, the  $E/B$  projectors mix contributions from regions with different  $\beta(q)$ . As a consequence, even though  $P_\nu$  is locally a pure power law, the projected fields  $P_{E,\nu}$  and  $P_{B,\nu}$  can exhibit non-trivial higher-order moments (effective spectral curvature in  $E$  and  $B$ ), frequency-dependent changes of the local polarization angle in the  $E$  and  $B$  maps, and hence a frequency-dependent  $E \leftrightarrow B$  balance. Only in the limiting case where  $\beta(q)$  is nearly constant on the angular scales to which  $L_E$  and  $L_B$  are most sensitive does one recover an approximately constant ratio  $|w_{n,E}|/|w_{n,B}|$ .

More generally, any effect that mixes power laws with different  $\beta$ , and in particular any effect that mixes pixels on the sphere, will tend to induce additional spectral complexity. This is the case for the  $E/B$  transform, but it would also arise for instrumental effects that mix neighbouring pixels, such as a finite-width beam (and especially when the beam size is larger than the typical scale of the  $\beta$  variations).

Since the illustration of the  $E/B$  transform loss-of-locality effect requires the knowledge of the whole field, we defer it to Sec. 4.

### 3.4 Intrinsic curvature and its superposition on the LoS

We now generalize the LoS superposition case presented in Sec. 3.2 to components with intrinsic curvature. Consider several components  $i$  along the line of sight with intrinsic log–Taylor curvature  $\gamma_i$ :

$$P_\nu = \sum_{i=1}^N P_{i,0} \exp[\beta_i s + \frac{1}{2} \gamma_i s^2] = P_0 \left( \frac{\nu}{\nu_0} \right)^{\bar{\beta}} C_{\gamma\text{LoS}}(\nu), \quad \text{where} \quad (48)$$

$$C_{\gamma\text{LoS}}(\nu) = \sum_{i=1}^N \frac{P_{i,0}}{P_0} \exp[(\beta_i - \bar{\beta})s + \frac{1}{2} \gamma_i s^2].$$

Using Eq. 31 one finds

$$w_0 = \sum_i P_{i,0}, \quad (49)$$

$$w_1 = \sum_i P_{i,0} (\beta_i - \bar{\beta}), \quad (50)$$

$$w_2 = \sum_i P_{i,0} [(\beta_i - \bar{\beta})^2 + \gamma_i]. \quad (51)$$

and using again the complex weighted average defined in Eq. 39,

$$\underline{\beta} = \left. \frac{d \log \underline{P}_\nu}{ds} \right|_0 = \langle \underline{\beta} \rangle, \quad (52)$$

$$\underline{\gamma} = \left. \frac{d^2 \log \underline{P}_\nu}{ds^2} \right|_0 = \langle \underline{\gamma} \rangle + (\langle \underline{\beta}^2 \rangle - \langle \underline{\beta} \rangle^2), \quad (53)$$

*i.e.* the effective curvature is the sum of the complex-weighted intrinsic curvatures average plus the complex-weighted variance of the spectral indices.

We illustrate in Fig. 2 the effect of curvature for the given (large) positive value of  $\gamma = 1$ : the SED amplitude becomes curved (*upper panel*) without affecting the fiducial input polarization angle (*lower panel*).

### 3.5 Synchrotron ageing

The classical relation between a power-law electron energy distribution and the optically thin synchrotron spectrum is given in Pacholczyk (1970); for  $N(E) \propto E^{-p}$ , the synchrotron flux density follows

$$S_\nu \propto \nu^{\alpha_{\text{inj}}}, \quad \text{where} \quad \alpha_{\text{inj}} = -\frac{p-1}{2}. \quad (54)$$

The global picture is that radiative losses progressively deplete high-energy electrons and produce a break in the spectrum at a characteristic frequency  $\nu_b$ . More precise and complicated treatments of spectral ageing are given in Murgia et al. (1999). For simplicity, we assume a simple smooth broken-power-law correction factor (relative to a high-frequency reference), given by

$$\underline{C}_{\text{age}}^{(\text{orig})}(\nu) = \left( \frac{\nu}{\nu_b} \right)^{\Delta\alpha} \left[ 1 + \left( \frac{\nu}{\nu_b} \right)^{1/\sigma} \right]^{-\sigma\Delta\alpha} \in \mathbb{R}, \quad (55)$$

where  $\Delta\alpha$  is the steepening of the spectral index and  $\sigma$  controls the sharpness of the break. This form is real-valued and thus does not affect polarization angles directly.

To ensure that the local complex spectral index at  $\nu_0$  is exactly  $\bar{\beta}$ , we renormalize this factor as

$$\underline{P}_\nu = \underline{P}_0 \left( \frac{\nu}{\nu_0} \right)^{\bar{\beta}} C_{\text{age}}(\nu), \quad \text{where} \quad (56)$$

$$C_{\text{age}}(\nu) = \frac{\left( \frac{\nu}{\nu_b} \right)^{\Delta\alpha} \left[ 1 + (\nu/\nu_b)^{1/\sigma} \right]^{-\sigma\Delta\alpha}}{\left( \frac{\nu_0}{\nu_b} \right)^{\Delta\alpha} \left[ 1 + (\nu_0/\nu_b)^{1/\sigma} \right]^{-\sigma\Delta\alpha}} \left( \frac{\nu}{\nu_0} \right)^{-\frac{\Delta\alpha}{1+(\nu_0/\nu_b)^{1/\sigma}}}.$$

Defining  $a \equiv (\nu_0/\nu_b)^{1/\sigma}$  and using  $s$  (see Eq. 10), this can be written compactly as

$$\log C_{\text{age}}(s) = \Delta\alpha \frac{a}{1+a} s - \Delta\alpha \sigma \log \frac{1+a e^{s/\sigma}}{1+a}. \quad (57)$$

The log–Taylor coefficients  $\underline{\kappa}_n$  are obtained by differentiating this expression. Using Eq. 27, the first two orders are

$$\underline{\beta} = \bar{\beta} + \left. \frac{d \log C_{\text{age}}}{ds} \right|_0 = \bar{\beta}, \quad (58)$$

$$\underline{\gamma} = \left. \frac{d^2 \log C_{\text{age}}}{ds^2} \right|_0 = -\frac{\Delta\alpha}{\sigma} \frac{a}{(1+a)^2}. \quad (59)$$

By construction  $(d \log C_{\text{age}}/ds)_{s=0} = 0$ , so the local slope at  $\nu_0$

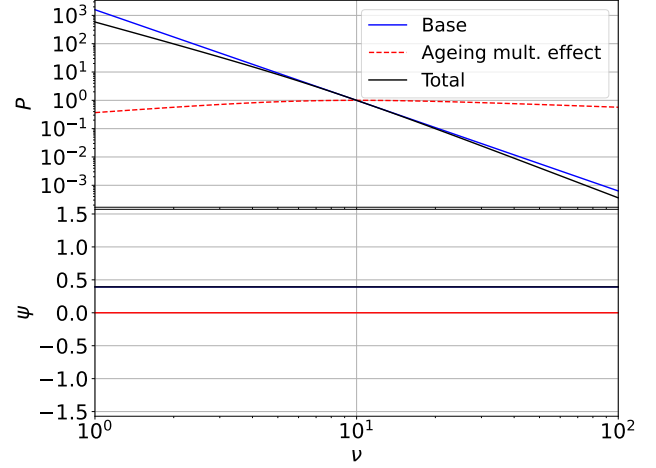


**Figure 3.** Example of the ageing effect (Sec. 3.5): Eq. 56 with  $\bar{\beta} = -3.2$ ,  $\sigma = 0.5$ ,  $\Delta\alpha = 1$  and  $\nu_b = 7$  GHz. The panels and curves are otherwise similar to the ones in Fig. 1.

equals  $\bar{\beta}$ , and all  $\underline{\kappa}_n$  are real. Applying Eq. 31 (with  $\underline{w}_0 = \underline{P}_0$ ) yields

$$\underline{w}_1^{(\text{age})} = \underline{w}_0 C'_{\text{age}}(0) = 0, \quad (60)$$

$$\underline{w}_2^{(\text{age})} = \underline{w}_0 C''_{\text{age}}(0) = -\underline{w}_0 \frac{\Delta\alpha}{\sigma} \frac{a}{(1+a)^2}. \quad (61)$$

The leading non-zero contribution is therefore a purely real second-order moment: ageing produces curvature in the amplitude spectrum, but no frequency-dependent angle evolution (no imaginary moments). Consequently,

$$\frac{|w_{n,E}^{(\text{age})}|}{|w_{n,B}^{(\text{age})}|} \approx \frac{|P_{0,E}|}{|P_{0,B}|} \quad (n \geq 0), \quad (62)$$

*i.e.*  $E/B$  ratios are preserved at all orders.

We illustrate in Fig. 3 the specific example of an aged SED (with given ageing parameters that are chosen to emphasize the effect), showing that ageing does not affect the angle (*lower panel*) and adds spectral complexity in the SED amplitude (*upper panel*).

### 3.6 Faraday effect

At low frequency the observed complex linear polarization  $\underline{P}_\nu$  is further modified by Faraday rotation and depolarization, which we encode in a complex propagation factor  $\underline{C}_{\text{FR}}(\lambda)$ , with  $\lambda = c/\nu$ . These effects arise from magneto-ionic material both co-spatial with the synchrotron-emitting region (internal Faraday rotation) and located in distinct foreground screens (external Faraday rotation).

For a uniform slab where synchrotron emission and Faraday rotation are co-spatial, Sokoloff et al. (1998, Eq. 34) showed that the complex polarization is multiplied by

$$\underline{C}_{\text{int}}(\lambda) = \frac{1 - \exp[-\underline{S}(\lambda)]}{\underline{S}(\lambda)}, \quad \underline{S}(\lambda) = 2\lambda^4 \sigma_{\text{RM,int}}^2 - 2i\lambda^2 \text{RM}_{\text{int}}, \quad (63)$$

where  $\text{RM}_{\text{int}} = K \int n_e B_{\parallel} dz$  is the internal Faraday depth in unit of Rotation Measure (RM) and  $\sigma_{\text{RM,int}}$  is the rms internal RM produced by small-scale magnetic fluctuations. The imaginary part of  $\underline{C}_{\text{int}}$  is responsible for differential Faraday rotation (phase), while the real part produces internal depolarization ( $\sim \exp[-\text{const}\lambda^4]$  in the strong-fluctuation limit).

A distinct external magneto-ionic screen contributes multiplicatively, see [Burn \(1966, Eqs. 23 and 25\)](#) or [Sokoloff et al. \(1998, Eq. B3\)](#):

$$\underline{C}_{\text{ext}}(\lambda) = \exp\left(-2\lambda^4\sigma_{\text{RM,ext}}^2 + 2i\lambda^2\text{RM}_{\text{ext}}\right) \quad (64)$$

with mean screen RM  $\text{RM}_{\text{ext}}$  and rms fluctuations  $\sigma_{\text{RM,ext}}$ . The first exponential is a pure phase (rotation), the second is a real depolarization factor.

The total Faraday factor is then

$$\underline{C}_{\text{FR}}^{(\text{orig})}(\lambda) = \underline{C}_{\text{int}}(\lambda) \underline{C}_{\text{ext}}(\lambda). \quad (65)$$

Writing

$$\underline{C}_{\text{int}}(\lambda) = A_{\text{int}}(\lambda) \exp[i\phi_{\text{int}}(\lambda)], \text{ and } \underline{C}_{\text{ext}}(\lambda) = A_{\text{ext}}(\lambda) \exp[i\phi_{\text{ext}}(\lambda)], \quad (66)$$

with

$$A_{\text{ext}}(\lambda) = \exp[-2\lambda^4\sigma_{\text{RM,ext}}^2], \quad \phi_{\text{ext}}(\lambda) = 2\lambda^2\text{RM}_{\text{ext}}, \quad (67)$$

$$A_{\text{int}}(\lambda) = |\underline{C}_{\text{int}}(\lambda)|, \quad \phi_{\text{int}}(\lambda) = \arg \underline{C}_{\text{int}}(\lambda), \quad (68)$$

the total amplitude and phase are

$$A_{\text{FR}}(\lambda) = A_{\text{int}}(\lambda) A_{\text{ext}}(\lambda), \text{ and } \phi_{\text{FR}}(\lambda) = \phi_{\text{int}}(\lambda) + \phi_{\text{ext}}(\lambda), \quad (69)$$

and the full correction factor is

$$\underline{C}_{\text{FR}}^{(\text{orig})}(\lambda) = A_{\text{FR}}(\lambda) \exp[i\phi_{\text{FR}}(\lambda)]. \quad (70)$$

An effective (freq.-dependent) rotation measure may be defined as

$$\text{RM}_{\text{eff}}(\lambda^2) \equiv \frac{1}{2} \frac{d\phi_{\text{FR}}}{d\lambda^2} = \text{RM}_{\text{ext}} + \frac{1}{2} \frac{d\phi_{\text{int}}}{d\lambda^2}, \quad (71)$$

so that in the absence of internal structure  $\text{RM}_{\text{eff}} \rightarrow \text{RM}_{\text{ext}}$ , while in general both internal and external contributions affect the total rotation and depolarization.

To ensure that the local spectral index at  $\nu_0$  equals  $\bar{\beta}$ , we again introduce a renormalized Faraday factor  $\underline{C}_{\text{FR}}(s)$  via

$$\underline{P}_\nu = \underline{P}_0 \left(\frac{\nu}{\nu_0}\right)^{\bar{\beta}} \underline{C}_{\text{FR}}(s), \quad \text{where} \quad (72)$$

$$\underline{C}_{\text{FR}}(s) = \frac{\underline{C}_{\text{FR}}^{(\text{orig})}(s)}{\underline{C}_{\text{FR}}^{(\text{orig})}(0)} \exp\left[-s \frac{d}{ds} \ln \underline{C}_{\text{FR}}^{(\text{orig})}(s) \Big|_{s=0}\right].$$

With this choice, applying Eq. 27 gives

$$\beta = \bar{\beta} + \frac{d \log \underline{C}_{\text{FR}}}{ds} \Big|_0 = \bar{\beta}, \quad (73)$$

while the curvature is in general complex:

$$\underline{\gamma} = \frac{d^2 \log \underline{C}_{\text{FR}}}{ds^2} \Big|_0 \quad (74)$$

$$= \underline{S}'_0 f(\underline{S}_0) + \underline{S}''_0 f'(\underline{S}_0) \quad (75)$$

$$- 32 \sigma_{\text{RM,ext}}^2 c^4 / \nu_0^4 + 8i \text{RM}_{\text{ext}} c^2 / \nu_0^2, \quad (76)$$

with

$$f(U) = \frac{e^{-U}}{1 - e^{-U}} - \frac{1}{U}, \text{ and } f'(U) = \frac{e^{-U}}{(1 - e^{-U})^2} + \frac{1}{U^2}, \quad (77)$$

and

$$\underline{S}_0 = 2\sigma_{\text{RM,int}}^2 (c/\nu_0)^4 - 2i \text{RM}_{\text{int}} (c/\nu_0)^2, \quad (78)$$

$$\underline{S}'_0 = -8\sigma_{\text{RM,int}}^2 (c/\nu_0)^4 + 4i \text{RM}_{\text{int}} (c/\nu_0)^2, \quad (79)$$

$$\underline{S}''_0 = 32\sigma_{\text{RM,int}}^2 (c/\nu_0)^4 - 8i \text{RM}_{\text{int}} (c/\nu_0)^2. \quad (80)$$

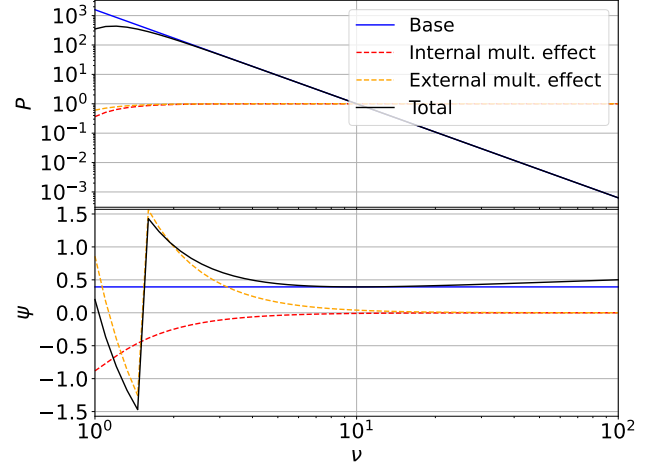


**Figure 4.** Example of the combination of internal and external Faraday effects (Sec. 3.6): Eq. 72 with  $\underline{P}_0 = e^{2i\pi/8}$ ,  $\bar{\beta} = -3.2$ ,  $\sigma_{\text{RM,int}} = \sigma_{\text{RM,ext}} = 0.5/c^2$ ,  $\text{RM}_{\text{int}} = -2/c^2$  and  $\text{RM}_{\text{ext}} = 4/c^2$ , with RMs expressed in units of  $\text{GHz}^2/c^2$ . The panels and curves are otherwise similar to the ones in Fig. 1 (for this particular illustration, (i) polarization angles are left unwrapped along  $\nu$  and are between  $[-\pi/2, \pi/2]$ , (ii) two distinct correction curves are represented, in red the internal Faraday effect and in orange the external Faraday effect).

Here  $\Re(\underline{\gamma})$  encodes Faraday-induced curvature of the amplitude spectrum (depolarization), while  $\Im(\underline{\gamma})$  encodes frequency-dependent rotation of the polarization angle.

From Eq. 31 (with  $\underline{w}_0 = \underline{P}_0$ ), the Faraday-induced moments are

$$\underline{w}_1^{(\text{FR})} = \underline{w}_0 \underline{C}'_{\text{FR}}(0) = 0, \quad (81)$$

$$\underline{w}_2^{(\text{FR})} = \underline{w}_0 \underline{C}''_{\text{FR}}(0) = \underline{w}_0 \underline{\gamma}, \quad (82)$$

which are also generically complex.

To see this more explicitly, consider the pure-rotation limit. The Faraday phase can then be written in terms of the effective rotation measure as

$$\Phi(\mathbf{n}) \equiv 2(c/\nu_0)^2 \text{RM}_{\text{eff}}(\mathbf{n}) = \bar{\Phi} + \delta\Phi(\mathbf{n}), \quad (83)$$

with  $\bar{\Phi}$  the sky-mean value and  $\delta\Phi$  the spatial fluctuations. A spatially uniform RM (*i.e.*  $\delta\Phi = 0$ ) preserves the zeroth-order  $E/B$  balance: for instance, in the specific case in which  $\underline{P}_{0,B} = 0$  then no  $B$  is generated by Faraday rotation alone. Instead, spatial variations  $\delta\Phi$  generate  $E/B$  mixing at first order in a small-rotation expansion (still in the specific example of  $\underline{P}_{0,B} = 0$ ):

$$\underline{w}_{1,E}^{(\text{FR})} \propto \bar{\Phi} \underline{w}_{0,E}, \text{ and } \underline{w}_{1,B}^{(\text{FR})} \propto \underline{L}_B[\delta\Phi \underline{w}_0], \quad (84)$$

so that

$$\frac{|\underline{w}_{1,E}^{(\text{FR})}|}{|\underline{w}_{1,B}^{(\text{FR})}|} \sim \frac{|\bar{\Phi} \underline{w}_{0,E}|}{|\underline{L}_B[\delta\Phi \underline{w}_0]|}. \quad (85)$$

An increase of  $|\underline{w}_{1,B}^{(\text{FR})}|/|\underline{w}_{1,E}^{(\text{FR})}|$  therefore signals frequency-dependent angle rotation sourced by spatial variations of  $\text{RM}_{\text{eff}}(\mathbf{n})$ .

Fig. 3 illustrates, for a specific choice of internal and external Faraday parameters, the impact of these effects on the spectral dependence of polarization. Depolarization manifests as a suppression of the SED amplitude at low frequencies (upper panel), while Faraday rotation produces a significant frequency-dependent rotation of

the polarization angle (lower panel), which approximately follows an inverse-square scaling with frequency<sup>3</sup>.

### 3.7 Coexistence of $E$ - and $B$ -dominated emitters and the impact of non-full-locality

As a final physical ingredient of particular interest (which is one of the motivations for working in  $E$ - and  $B$ - separated fields), we consider the coexistence of spatial features that are intrinsically  $E$ - or  $B$ -dominated and that have different spectral indices, ageing signatures, or Faraday properties. When such components are approximately separable in morphology, their contributions to the moment maps are correspondingly separable.

For example, consider two co-located components  $\underline{P}_a$  ( $E$ -like, index  $\beta_a$ ) and  $\underline{P}_b$  ( $B$ -like, index  $\beta_b$ ). At first order,

$$\underline{w}_1 \simeq \underline{P}_a(\beta_a - \bar{\beta}) + \underline{P}_b(\beta_b - \bar{\beta}), \quad (86)$$

and, provided the templates are approximately pure  $E$  or  $B$ ,

$$\underline{w}_{1,E} \simeq \underline{P}_a(\beta_a - \bar{\beta}), \quad \underline{w}_{1,B} \simeq \underline{P}_b(\beta_b - \bar{\beta}), \quad (87)$$

so that

$$\frac{|\underline{w}_{1,E}|}{|\underline{w}_{1,B}|} \simeq \frac{|\underline{P}_a| |\beta_a - \bar{\beta}|}{|\underline{P}_b| |\beta_b - \bar{\beta}|}. \quad (88)$$

In this regime the first spectral moment directly traces the relative spectral slopes of the  $E$ - and  $B$ -producing structures.

It is important to note, however, that as discussed in Sec. 3.3 and Appendix B, the operators  $\underline{L}_E$ ,  $\underline{L}_B$ , and  $\underline{L}_S$  act as finite-width convolutions on the sphere. Consequently, the projected fields  $\underline{P}_E(\mathbf{n})$  and  $\underline{P}_B(\mathbf{n})$  at a given direction receive contributions from neighbouring structures with potentially different spectral properties. This non-fully-local mixing slightly blurs the naive picture of perfectly separable “ $E$ -emitters” and “ $B$ -emitters”, and motivates treating the spectral properties of  $\underline{P}_E$  and  $\underline{P}_B$  as observables in their own right.

## 4 VERIFICATION OF PREDICTIONS AND INTERPRETABILITY OF THE FIELDS

Because the spectral complexity induced in  $\underline{P}_E$ ,  $\underline{P}_B$  and  $\underline{S}$  depends in a non-fully-local way on the full-sky morphology, quantitative predictions for these transformed fields can only be made once a concrete sky model is specified. In this section we therefore move from the general mechanisms discussed in Sec. 3 to explicit examples. In Sec. 4.1, we construct a controlled toy model that allows us to verify the superposition, ageing and Faraday predictions derived previously, and to investigate how these effects impact the interpretability of  $\underline{P}_E$ ,  $\underline{P}_B$  and  $\underline{S}$ . This sets the stage for the more realistic PySM-based analysis presented in Sec. 4.2.

### 4.1 Simple toy model

We first consider a simple eight-component toy model with varying  $E/B$  balance and spectral properties. The components are chosen to span a range of morphologies (loops, circular sources, stochastic-angle structures) and physical mechanisms (pure spectral power laws, intrinsic spectral curvature, ageing, Faraday effects). We present its

	$E/B$	$A$	$\beta$	Other prop.
(1) E loop	$+\infty$	1	-3.4	–
(2) B loop	0	1	-2.6	–
(3) Random-angle galaxy	rand ( $5^\circ$ )	1	-3.0	–
(4) Circular source	0	1	-3.2	Aged
(5) Circular source	1	1	-3.2	$\gamma > 0$
(6) Circular source	$+\infty$	1	-3.2	Faraday
(7) Stochastic-angle stripe	rand ( $20^\circ$ )	1	-2.8	–
(8) Random-angle bg.	rand ( $20^\circ$ )	0.01	-3.0	–

**Table 1.** Components included in the toy model. The numbering corresponds to the labels in the polarization–amplitude panel of Fig. 5 (top row, centre). The first column indicates the relative contribution of each feature to  $E$  and  $B$ , while the second gives the relative total polarization amplitude, which unit does not matter for the discussion. In the spectral analysis of Sec. 4.1.2, these two morphological columns are defined at the pivot frequency of 10 GHz, together with the two spectral columns used to extrapolate the model to lower and higher frequencies: the third column is the spectral index at 10 GHz and the fourth column specifies whether a more complicated spectral property is considered beyond the simple power law ( $\gamma > 0$  meaning positively curved).

morphology at the reference frequency in Sec. 4.1.1 and analyse its spectral properties in Sec. 4.1.2, thereby validating the prediction equations derived in Sec. 3. We then use the toy model in Sec. 4.1.3 to illustrate how spectral conclusions can be drawn from the various  $E/B$ -separated fields, before showing in Sec. 4.1.4 the complementarity of the two types of spectral expansion considered in this work.

#### 4.1.1 Central-frequency morphology

The properties of the eight components of the toy model are summarized in Table 1. In order to obtain a band-limited toy model, for which harmonic-space transformations can be applied consistently, we first construct the morphology in pixel space and then apply a harmonic-space cut, removing all modes above  $\ell_{\max} = 3N_{\text{side}} - 1$ , where  $N_{\text{side}} = 512$  is the HEALPix resolution parameter of the toy model<sup>4</sup>. The obtained  $(Q, U, P, \psi)$  morphology is illustrated in the first row of Fig. 5, where we have overlaid the identification number of each component on the  $P$  map. The second and third rows display the corresponding  $E$ - and  $B$ -family fields  $(Q_E, U_E, P_E, \psi_E)$  and  $(Q_B, U_B, P_B, \psi_B)$  obtained through the map-space  $E/B$  decomposition introduced in Sec. 2. Finally, the last column of Fig. 5 shows the  $P_E$  to  $P_B$  ratio as well as the  $E$  and  $B$  scalar maps (from upper panel to lower panel).

Several key features are immediately apparent. Purely  $E$ -type structures (components 1 and 6) disappear from the  $B$ -family panels, while purely  $B$ -type structures (component 2) vanish from the  $E$ -family fields. Sources with mixed morphology or stochastic angles (components 3, 5, 7, 8) appear in both families, as expected. The map of the local ratio  $P_E/P_B$  (top-right panel) clearly separates radial-like ( $E$ -dominated) from solenoidal ( $B$ -dominated) patterns and highlights regions where a single component dominates the local  $E/B$  balance. This matches the conceptual picture of Sec. 2:  $\underline{P}_E$  and  $\underline{P}_B$  retain the spin-2 nature of the field (contrary to scalar  $E$ ,  $B$ ,  $\underline{S}$ ) while efficiently isolating gradient- and curl-like contributions (contrary to  $\underline{P}$ ).

<sup>3</sup> We note that, over most of the parameter space of this model, the onset of noticeable rotation occurs at higher frequencies than that of significant depolarization.

<sup>4</sup> This procedure may induce a very small loss of locality, and hence a negligible amount of associated spectral complexity, but it is required to ensure the consistency of the harmonic transforms and, in particular, to preserve the closure relation.

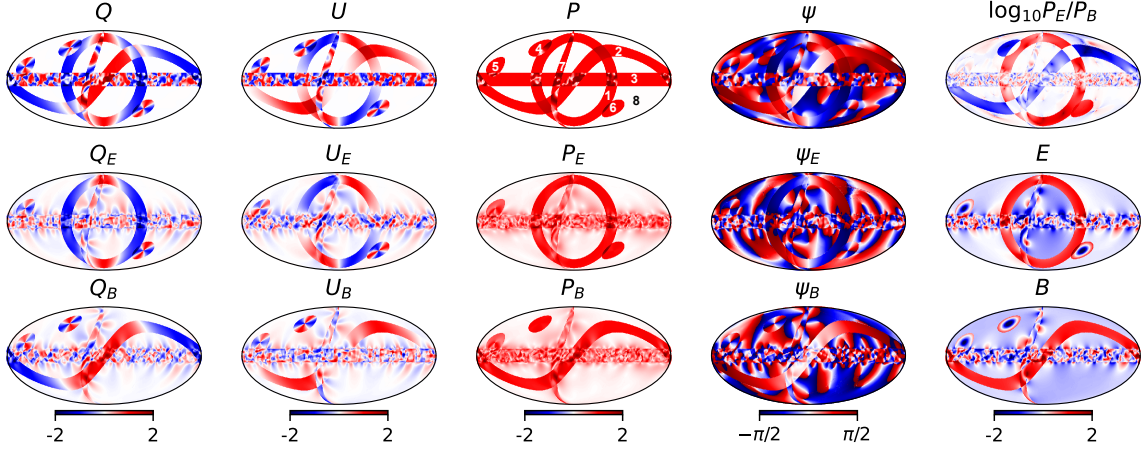


**Figure 5.** Toy-model polarization sky at a single frequency. The numbered structures in the total polarization amplitude panel (top row, centre) correspond to the components defined in Table 1, each chosen to illustrate a distinct  $E/B$  balance and morphology. The first row shows the full Stokes fields ( $Q, U$ ) together with the resulting total polarization amplitude  $P$  and angle  $\psi$ . The second and third rows display the corresponding  $E$ - and  $B$ -family fields ( $Q_E, U_E, P_E, \psi_E$ ) and ( $Q_B, U_B, P_B, \psi_B$ ) obtained through the map-space  $E/B$  decomposition.

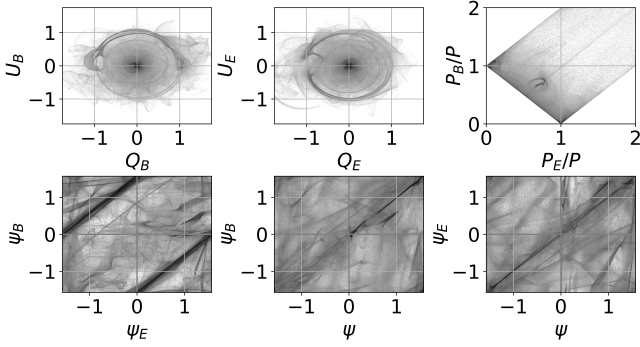


**Figure 6.** Two-dimensional distributions of several pairs of map-level quantities derived from the toy model. The first row shows the  $(Q_B, U_B)$  and  $(Q_E, U_E)$  planes, while the second row displays the planes  $(P_E/P, P_B/P)$ ,  $(\psi_E, \psi_B)$ , and  $(\psi, \psi_E)$ , all evaluated at the reference frequency of 10 GHz. The grey-scale density displays the pixel counts in log scale, in each parameter space.

Fig. 6 complements this map-space view with two-dimensional distributions. The  $(Q_B, U_B)$  and  $(Q_E, U_E)$  planes (*upper-left* and *upper-middle*) show how the  $E/B$  decomposition projects each pixel into its  $E$ -family or  $B$ -family Stokes components. Purely  $E$ - or  $B$ -type structures cluster in compact regions of their respective planes, while mixed or stochastic components populate broader domains. The  $(P_E/P, P_B/P)$  plane (*upper-right*) directly visualizes the constraint  $(P_E - P_B)^2 < P^2 < (P_E + P_B)^2$  derived in Eq. 24: the pixel distribution is confined to the allowed region, with  $E$ -dominated pixels lying near the  $(P_E/P, P_B/P) \simeq (1, 0)$  corner and  $B$ -dominated pixels near  $(P_E/P, P_B/P) \simeq (0, 1)$ . The angular (*lower*) planes  $(\psi_E, \psi_B)$ ,  $(\psi, \psi_B)$ , and  $(\psi, \psi_E)$  reveal that regions containing a single dominant morphological component lie close to the diagonal, whereas pixels combining multiple structures with different orientations fill larger areas of these plots.

Taken together, Figs. 5 and 6 illustrate how the  $E/B$  decomposition reorganizes the polarization field both in map space and in the  $(Q, U)$ ,  $(P_E/P, P_B/P)$  and angle planes. They also provide a con-

crete playground in which to apply the spectral predictions derived in Sec. 3.

#### 4.1.2 Verifying spectral predictions

We now extend the toy model to multiple frequencies by assigning specific spectral behaviours to the components, as indicated in the last column of Table 1. The circular source (4) is affected by synchrotron ageing with the parameters used for Fig. 3:  $\bar{\beta} = -3.2$ ,  $\sigma = 0.5$ ,  $\Delta\alpha = 1$  and  $\nu_b = 7$  GHz. The circular source (5) has intrinsic curvature with  $\bar{\beta} = -3.2$  and  $\gamma = 1$  (Fig. 2). The circular source (6) is affected by internal and external Faraday effects with  $\bar{\beta} = -3.2$ ,  $\sigma_{\text{RM,int}} = \sigma_{\text{RM,ext}} = 0.5/c^2$ ,  $\text{RM}_{\text{int}} = -2/c^2$  and  $\text{RM}_{\text{ext}} = 4/c^2$  (Fig. 4). The remaining components follow simple power laws with the spectral indices listed in Table 1.

Using the combination rules of Eqs. 32–34, the moments of the total polarization field in this eight-component model are

$$\underline{w}_0 = \sum_{i=1}^8 \underline{A}_i, \quad (89)$$

$$\underline{w}_1 = \sum_{i=1}^8 \underline{A}_i \Delta\beta_i, \quad (90)$$

$$\underline{w}_2 = \sum_{i=1}^8 \underline{A}_i \left[ \Delta\beta_i^2 + \gamma_i + C_{2,i}^{(\text{age})} + C_{2,i}^{(\text{FR})} \right], \quad (91)$$

where  $\underline{A}_i$  is the complex amplitude of component  $i$  at  $\nu_0$ ,  $\Delta\beta_i \equiv \beta_i - \bar{\beta}$ , and  $C_{2,i}^{(\text{age})}$  and  $C_{2,i}^{(\text{FR})}$  are the second-order (real and complex) contributions from ageing and Faraday effects as given in Secs. 3.5 and 3.6. The effective log–Taylor coefficients of the total field then follow from Eq. 17.

We compare these analytic predictions with parameters fitted directly to simulated maps at three frequencies<sup>5</sup>. To isolate purely

<sup>5</sup> Hereafter, we fix the reference  $\bar{\beta}$  of the moment expansion to  $-3$ , close to the average-sky  $\beta$  by construction of all sky models studied hereafter. We verified that as long as this reference is only slightly varied, the reliability of the predictions is not affected and the performance of the moment extrapolation is only weakly affected.

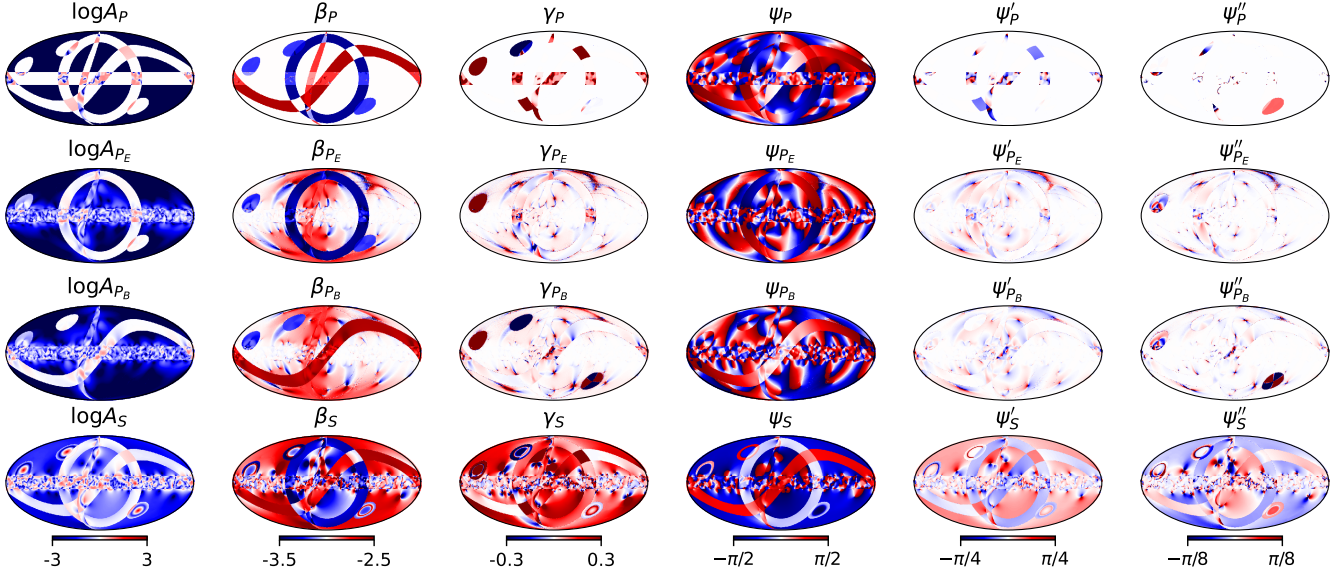


**Figure 7.** Maps of complex log–Taylor parameters for the toy model, for  $\underline{P}$  (top row),  $\underline{P}_E$  (second row),  $\underline{P}_B$  (third row) and  $\underline{S}$  (bottom row). Columns show  $\log A_X$ ,  $\psi_X$ ,  $\beta_X$ ,  $\psi'_X$ ,  $\gamma_X$  and  $\psi''_X$  (from left to right), where primes denote derivatives with respect to  $s$  (cf. Eq. 10). The colorbar of a given column is common to all rows and provided at the bottom of the figure. Angular fields are given in radians.

numerical effects, we first use three very closely spaced channels,  $\nu_a = 9.999$  GHz,  $\nu_b = \nu_0 = 10$  GHz and  $\nu_c = 10.001$  GHz<sup>6</sup>.

In this regime the moments and log–Taylor parameters fitted on  $\underline{P}$  agree with the one predicted from Eqs. 89–91 and Eq. 17 to better than  $10^{-5}$  relative accuracy. We illustrate this comparison in map space in Appendix C. This confirms that the expressions derived in Sec. 3 correctly capture the behaviour of the complex field under line-of-sight superposition, intrinsic curvature, ageing and Faraday rotation, when evaluated near the pivot frequency.

We repeat the same exercise for the  $E$ - and  $B$ -family fields and for the scalar field  $\underline{S}$ . One approach is to fit log–Taylor parameters directly to  $\underline{P}_E$ ,  $\underline{P}_B$  or  $\underline{S}$  at the three frequencies. Alternatively, we can (i) predict the  $\underline{P}$  moments using Eqs. 89–91, (ii) map these to moments for  $\underline{P}_E$ ,  $\underline{P}_B$  and  $\underline{S}$  using the linear relations of Eq. 21, and (iii) convert the resulting moments to log–Taylor parameters via Eq. 17. The two procedures agree to within  $10^{-4}$  relative accuracy, thereby validating the combination of (a) the physical predictions for the  $\underline{P}$  moments, (b) the moment–log–Taylor conversion, and (c) the linear  $E/B$  projection relations established in Sec. 2.

#### 4.1.3 Spectral conclusions on the toy model in $\underline{P}$ , $\underline{P}_E$ , $\underline{P}_B$ and $\underline{S}$

We now use the multi-frequency toy model to compare the spectral behaviour of the different fields  $\underline{P}$ ,  $\underline{P}_E$ ,  $\underline{P}_B$  and  $\underline{S}$ . This serves three purposes: it illustrates the physical mechanisms discussed in Sec. 3, proposes various diagnostics that are meaningful to apply to data, and anticipates the tendencies that will reappear in the more realistic

<sup>6</sup> As one expects, using three frequencies to fit a model with only three complex parameters limits the validity of the fit away from  $\nu_0$ , especially in regions where higher-order spectral parameters are non-negligible (e.g., in the vicinity of the curved or Faraday-active sources). A low-order expansion around  $s = 0$  provides an accurate local description, but cannot perfectly reproduce spectral properties far from the pivot. To illustrate this, more realistically spaced frequency channels will be considered in Sec. 4.1.4.

PySM simulations. We focus on four aspects: (i) the stability of the polarization angle (Sec. 4.1.3.1), (ii) generalized  $E/B$  ratios at different spectral orders (Sec. 4.1.3.2), (iii) direct comparisons of log–Taylor parameters between  $E$  and  $B$  (Sec. 4.1.3.3), and (iv) simple diagnostics of spectral complexity (Sec. 4.1.3.4). All quantities below can be computed either from the moments  $\underline{w}_n$  or from the associated complex log–Taylor coefficients and are illustrated in Figs. 7 and 8.

**4.1.3.1 Angle stability in  $\underline{P}$ ,  $\underline{P}_E$  and  $\underline{P}_B$**  As discussed in Sec. 2.2.3, the imaginary parts of the complex log–Taylor coefficients control the evolution of the polarization angle with frequency:  $\frac{1}{2}\Im(\beta)$  and  $\frac{1}{2}\Im(\gamma)$  correspond to the first and second derivatives of  $\psi$  with respect to  $s$ . In practice, all angles reported hereafter are unwrapped (using the `unwrap` function of `numpy`), which also ensures a robust determination of the frequency evolution of the angles.

In the total polarization  $\underline{P}$  (top row of Fig. 7), the angle derivatives  $\psi'_P$  and  $\psi''_P$  are close to zero over most of the sky. Significant deviations occur only where components with different intrinsic angles and non-trivial spectra overlap, notably around the Faraday-active circular source (6) and, more mildly, near intersections of the large  $E$  and  $B$  loops (1 and 2) with the stochastic-angle structures (3, 7, 8). This behaviour directly reflects the mechanisms of Sec. 3.2 and 3.6: angle evolution in  $\underline{P}$  arises either from line-of-sight mixing of misaligned power laws or from Faraday rotation.

By contrast, the projections  $\underline{P}_E$  and  $\underline{P}_B$  (second and third rows) present much richer patterns in  $\psi'_X$  and  $\psi''_X$ . The  $E$  projection enhances angle variations along the large  $E$  loop and the stochastic galactic band, while the  $B$  projection concentrates strong derivatives along the  $B$  loop and around the aged and Faraday circular sources (4–6). Even when  $\psi'_P$  is small, the derivatives of  $\psi_{P_E}$  and  $\psi_{P_B}$  can be substantial. This illustrates a key point anticipated in Sec. 3: the map-space  $E/B$  transform redistributes the same physical effects into different parity channels through non-fully-local kernels, so a modest frequency dependence of the total angle can correspond to a much more significant angle evolution in  $\underline{P}_E$  and  $\underline{P}_B$ .

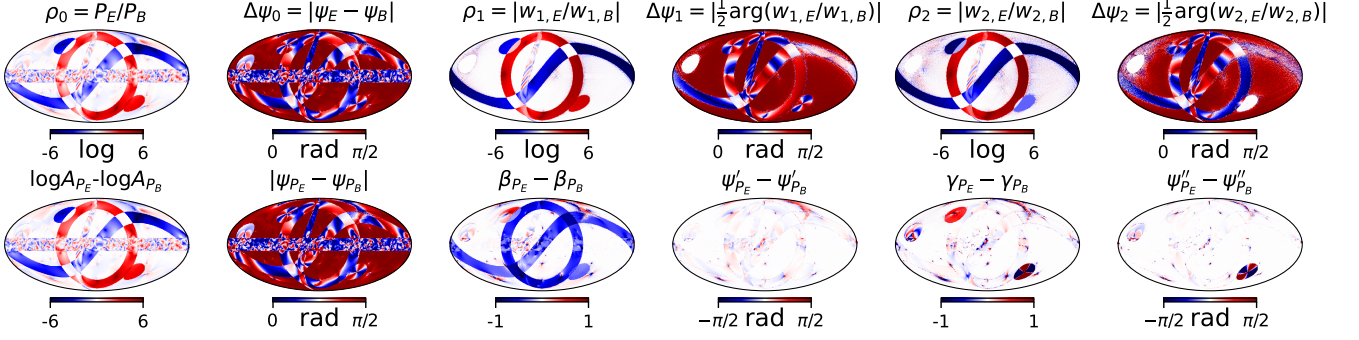


**Figure 8.** Generalized  $E/B$  diagnostics for the toy model. *Upper panels:* maps of  $\rho_n = |w_{n,E}/w_{n,B}|$  and  $|\Delta\psi_n| = \frac{1}{2} |\arg(w_{n,E}/w_{n,B})|$  for  $n = 0, 1, 2$ . *Lower panels:* differences between  $E$  and  $B$  log–Taylor parameters, namely  $\log A_{P_E} - \log A_{P_B}$ ,  $|\psi_{P_E} - \psi_{P_B}|$ ,  $\beta_{P_E} - \beta_{P_B}$ ,  $\psi'_{P_E} - \psi'_{P_B}$ ,  $\gamma_{P_E} - \gamma_{P_B}$ , and  $\psi''_{P_E} - \psi''_{P_B}$ .

The scalar field  $\underline{S}$  (*lower panels*) shows yet another behaviour: its angle and angle derivatives vary smoothly on large scales set by the loops and band but are rarely close to zero. This is consistent with the expectation that  $\underline{S}$  combines amplitude and angle in a non-linear way, and therefore tends to exhibit enhanced spectral complexity.

Angle stability provides a first diagnostic of *spectral complexity*. A field with small absolute values of  $\psi'_X$  and  $\psi''_X$  can be accurately extrapolated using simple rigid-angle (i.e. amplitude-only) models, and also indicates a morphology that remains stable across frequencies, making such fields well suited for modelling the physics of polarized emission over the sky.

**4.1.3.2 Generalized  $E/B$  ratios** To quantify how the  $E/B$  balance evolves with spectral order, we introduce

$$\rho_n = \left| \frac{w_{n,E}}{w_{n,B}} \right|, \quad \Delta\psi_n = \frac{1}{2} \arg \left[ \frac{w_{n,E}}{w_{n,B}} \right], \quad (92)$$

where  $w_{n,E}$  and  $w_{n,B}$  are the  $n$ -th moments of  $\underline{P}_E$  and  $\underline{P}_B$ . The ratio  $\rho_n$  measures the amplitude balance between  $E$  and  $B$  at order  $n$ , while  $\Delta\psi_n$  measures the relative phase. When  $\Delta\psi_n \simeq 0$ , the  $E$  and  $B$  contributions at order  $n$  share a similar angle evolution; when  $|\Delta\psi_n| \sim \pi/2$ , their contributions are nearly orthogonal in the complex plane. In that sense,  $\{\rho_n, \Delta\psi_n\}$  provide a natural generalization of the familiar map-level ratio  $\underline{P}_E/\underline{P}_B$  discussed in Sec. 2.

Fig. 8 shows  $\rho_n$  and  $|\Delta\psi_n|$  for  $n = 0, 1, 2$ . For  $n = 0$ ,  $\rho_0$  reproduces the single-frequency  $E/B$  amplitude ratio. The large  $E$  loop (1) appears as strongly  $E$ -dominated, the large  $B$  loop (2) as strongly  $B$ -dominated, while the stochastic-angle components (3, 7, 8) and the intrinsically  $E/B$ -balanced circular source (5) populate intermediate values. The corresponding angle difference  $|\Delta\psi_0| = |\psi_E - \psi_B|$  is small only where a single component dominates; elsewhere it is close to  $\pi/2$ , reflecting the fact that  $E$  and  $B$  spin-2 objects in this model are mostly perpendicular in the background region.

This behaviour can be understood from the combination of the closure relation Eq. 9 and the non-fully-local nature of the  $E/B$  projectors. By construction, the pure fields obey  $\underline{P} = \underline{P}_E + \underline{P}_B$  at every pixel. In the background region of the toy model the “true” polarization  $\underline{P}$  is very small (only the weak stochastic component is present), whereas the non-fully-local  $E/B$  transform spreads the signal from the bright structures over a much wider area. The tails of this response are therefore carried almost entirely by  $\underline{P}_E$  and  $\underline{P}_B$ , which must satisfy  $\underline{P}_E(\mathbf{n}) \simeq -\underline{P}_B(\mathbf{n})$  wherever  $\underline{P}(\mathbf{n}) \simeq 0$ . In terms of Stokes parameters this implies  $Q_B \simeq -Q_E$  and  $U_B \simeq -U_E$ , and

hence  $2\psi_B \simeq 2\psi_E + \pi$ , i.e.  $\psi_B \simeq \psi_E + \pi/2$ . The near-orthogonality of the  $E$ - and  $B$ -polarization orientations in the background is thus not an independent physical feature of the sky, but the natural way in which the non-fully-local  $E/B$  decomposition enforces  $\underline{P} = \underline{P}_E + \underline{P}_B$  in regions where the input polarization is intrinsically weak.

At  $n = 1$ ,  $\rho_1$  compares the first-order spectral gradients of  $E$  and  $B$ . Regions where components with distinct spectral indices overlap (e.g., intersections of loops, galaxy and stripe) stand out more clearly in  $\rho_1$  than in  $\rho_0$ , indicating that first-order departures from a power law are preferentially carried by either gradient-like or curl-like structures depending on the local composition. This is precisely the behaviour anticipated in Sec. 3.3 and 3.2, where spatially varying  $\beta$  and line-of-sight superposition were shown to generate non-zero  $w_1$ . The corresponding  $|\Delta\psi_1|$  shows that, even when the static  $E/B$  patterns are asymmetric, the angle evolution of the  $E$  and  $B$  gradients can remain relatively aligned in some regions, but is strongly decorrelated in others, especially around the Faraday source (6) where complex  $\underline{\gamma}$  is expected.

For  $n = 2$ ,  $\rho_2$  is dominated by the three curved components (4–6). The aged  $B$ -like circular source (4), the intrinsically curved  $E/B$ -balanced source (5) and the Faraday-rotated  $E$ -like source (6) appear as localized features with distinct signs and amplitudes depending on whether curvature is stronger in  $E$  or in  $B$ . The rest of the sky, where the spectra are close to power laws, contributes little to  $\rho_2$ . The angle difference  $|\Delta\psi_2|$  is small for the intrinsically curved source (5), where  $E$  and  $B$  acquire similar curvature in angle, but large around the Faraday region (6), where the curvature of the  $B$ -mode angle is much stronger than that of  $E$ , in line with the Faraday-mixing picture of Sec. 3.6.

**4.1.3.3 Log–Taylor parameters per field** The *bottom row* of Fig. 8 summarizes the same information directly in terms of differences between  $E$ - and  $B$ -mode log–Taylor parameters:  $\log A_{P_E} - \log A_{P_B}$ ,  $|\psi_{P_E} - \psi_{P_B}|$ ,  $\beta_{P_E} - \beta_{P_B}$ ,  $\psi'_{P_E} - \psi'_{P_B}$ ,  $\gamma_{P_E} - \gamma_{P_B}$  and  $\psi''_{P_E} - \psi''_{P_B}$ . The first two maps essentially reproduce  $\rho_0$  and  $|\Delta\psi_0|$ . The difference  $\beta_{P_E} - \beta_{P_B}$  highlights where effective spectral indices differ between  $E$  and  $B$ : large positive and negative values are found on the pure  $E$  and  $B$  loops (1 and 2), while the stochastic background (8) shows values close to zero, consistent with nearly symmetric  $E/B$  contributions.

The difference in angle gradients,  $\psi'_{P_E} - \psi'_{P_B}$ , is generally modest, confirming that to first order the angle evolution in  $E$  and  $B$  is often similar, except around regions where several mechanisms combine,

such as the Faraday-active source (6) and overlap zones of multiple components. The curvature differences  $\gamma_{P_E} - \gamma_{P_B}$  and  $\psi''_{P_E} - \psi''_{P_B}$  isolate precisely the regions where second-order behaviour differs between the two parities; they are dominated by the  $B$  aged and  $E$  Faraday rotated circular sources (4–6).

**4.1.3.4 Spectral complexity** Finally, we use the moments and log–Taylor parameters to characterize spectral complexity, understood as the departure from a spatially uniform power law. For each field  $X \in \{\underline{P}, \underline{P}_E, \underline{P}_B, \underline{S}\}$  one can define, for example,  $C_{1,X} = \left| \frac{w_{1,X}}{w_{0,X}} \right|$  and  $C_{2,X} = \left| \frac{w_{2,X}}{w_{0,X}} \right|$ , or, equivalently, use the spatial structure and amplitude of  $\beta_X$  and  $\gamma_X$  in Fig. 7.

In this toy model, the total polarization  $\underline{P}$  is globally less spectrally complex than its  $E$  and  $B$  projections:  $\beta_P$  and  $\gamma_P$  show large regions that are nearly uniform or close to zero, whereas  $\beta_{P_E}$ ,  $\beta_{P_B}$  and especially  $\gamma_{P_E}$  and  $\gamma_{P_B}$  display more small-scale structure, particularly along the galactic band and in overlap regions of multiple components. This is consistent with the idea that the  $E/B$  projections, being non-fully-local, effectively superpose contributions with different spectral behaviours (Sec. 3.2), thereby enhancing higher-order moments. However, the toy model also shows that this trend is not universal: in patches dominated by a single curved component (*e.g.*, inside the bright parts of the loops or circular sources), the spectral gradients and curvatures of  $\underline{P}$ ,  $\underline{P}_E$  and  $\underline{P}_B$  can be comparable.

A more robust conclusion emerges for the scalar field  $\underline{S}$ . Its maps of  $\beta_S$  and  $\gamma_S$  (bottom row of Fig. 7) exhibit strong variations and ring-like structures around essentially all components, and the corresponding angle derivatives are rarely close to zero. Intuitively,  $\underline{S}$  mixes amplitude and angle into a single scalar quantity, so any change in either with frequency increases its effective complexity. In this toy model  $\underline{S}$  is systematically more complex, both in gradient and curvature, than the underlying spin-2 fields  $\underline{P}$ ,  $\underline{P}_E$  and  $\underline{P}_B$ . This empirical observation strengthens the conceptual arguments of Sec. 2: from the point of view of spectral modelling and physical interpretation,  $\underline{P}_E$  and  $\underline{P}_B$  provide a more natural and transparent description than the scalar combination  $\underline{S}$ .

We stress that these conclusions are drawn from an idealized and highly structured toy sky. The quantitative balance between  $\underline{P}$ ,  $\underline{P}_E$ ,  $\underline{P}_B$  and  $\underline{S}$  will depend on the actual morphology and physical content of the Galactic foregrounds. Nevertheless, the toy model usefully validates the theoretical framework of Sec. 3 and illustrates diagnostics one can use. In practice, spectral-complexity diagnostics, such as the present test or the angle-stability test described in Sec. 4.1.3.1, can be applied to real data to identify representations that are less costly to model and that exhibit stable morphology across frequencies.

#### 4.1.4 Performance with a finite number of frequency channels

In order to assess how well the different spectral parametrizations recover the underlying frequency dependence when only a few channels are available, we designed the following test on the toy model. We select three frequencies,  $\nu_0 = 10$  (the pivot) and  $\nu = \{5, 15\}$ , and evaluate the full toy model at these three frequencies to obtain the “truth” maps for the complex polarization fields  $\underline{P}$ ,  $\underline{P}_E$ ,  $\underline{P}_B$ , which are the focus of this discussion.

For each field  $\underline{X} \in \{\underline{P}, \underline{P}_E, \underline{P}_B\}$ , we then use the map-space predictions for its second-order complex log–Taylor parameters or complex moments (predictions that we have derived in Sec. 3 and validated in Sec. 4.1.2 in the near-frequencies setup) to extrapolate the pivot-frequency value  $\underline{X}_{\nu_0}$  to  $\nu = \{5, 15\}$  (with SEDs Eqs. 12 or 15 *resp.* for the log–Taylor or moment expansions). This yields approximate

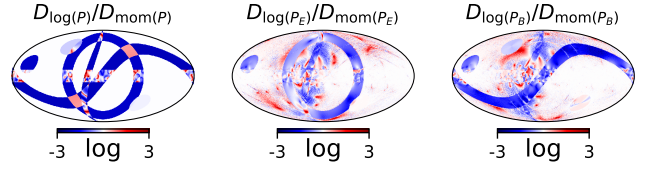


**Figure 9.** Maps of the decimal logarithm of the ratio between the log–Taylor and moment reconstruction errors, evaluated at  $\nu = \{5, 10, 15\}$  GHz with pivot  $\nu_0 = 10$  GHz. From left to right the panels show  $\log_{10}[D_{\log(P)}/D_{\text{mom}(P)}]$ ,  $\log_{10}[D_{\log(P_E)}/D_{\text{mom}(P_E)}]$  and  $\log_{10}[D_{\log(P_B)}/D_{\text{mom}(P_B)}]$ , where  $D_X$  is defined by Eq. 93.

model maps  $\underline{X}_{\nu}^{\text{model}}$  based on (i) a truncated log–Taylor expansion and (ii) a truncated moment expansion, each retaining three spectral parameters per pixel.

The quality of these reconstructions is quantified thanks to the criterion defined by Eq. (25) of Chluba et al. (2017), that we generalize to complex polarization fields. For a given complex field  $\underline{X}_{\nu}$  and its approximation  $\underline{X}_{\nu}^{\text{model}}$ , we define

$$D_{\underline{X}} = \sqrt{\frac{1}{N_{\text{ch}}} \sum_{i=1}^{N_{\text{ch}}} \left| \frac{\underline{X}_{\nu_i}^{\text{model}}}{\underline{X}_{\nu_i}^{\text{input}}} - 1 \right|^2}, \quad (93)$$

where the sum runs over the three frequency channels and the modulus is in the complex plane. Applied to the second-order log–Taylor and moment models in the three fields, this yields per-pixel maps  $D_{\log(P)}$  and  $D_{\text{mom}(P)}$ ,  $D_{\log(P_E)}$  and  $D_{\text{mom}(P_E)}$ , and  $D_{\log(P_B)}$  and  $D_{\text{mom}(P_B)}$ .

Fig. 9 displays the decimal logarithm of the ratio between the log–Taylor and moment errors,  $\log_{10}\left[\frac{D_{\log(P)}}{D_{\text{mom}(P)}}\right]$ ,  $\log_{10}\left[\frac{D_{\log(P_E)}}{D_{\text{mom}(P_E)}}\right]$  and  $\log_{10}\left[\frac{D_{\log(P_B)}}{D_{\text{mom}(P_B)}}\right]$ , for the three complex fields. Blue regions correspond to  $D_{\log} < D_{\text{mom}}$ , *i.e.* a better reconstruction from the log–Taylor parametrization, while red regions indicate the opposite.

For this particular toy model and choice of physical components, the log–Taylor expansion systematically outperforms the whole-sky–referenced moment expansion when both are truncated at second order and constrained by only three frequency channels. This trend is seen consistently in  $\underline{P}$ ,  $\underline{P}_E$  and  $\underline{P}_B$ , suggesting that, in this regime, the complex log–Taylor description is better suited to capture the detailed spectral behaviour of the polarized sky than the corresponding low-order moment expansion around a single reference index  $\bar{\beta}$ .

This result would differ if one were to define a reference spectral index  $\bar{\beta}$  on a pixel-by-pixel basis (for instance as the mean spectral index of the components along the line of sight). Such a choice, however, would break the full-sky linearity of the moment expansion, which is a key property exploited throughout this work. The quantitative outcome is also sensitive to the details of the toy model, in particular to the number of components along the line of sight, as well as to the choice and spacing of the frequency channels. For example, Chluba et al. (2017) showed that, when more spectral parameters and more observing frequencies are available, the (real) moment expansion converges more rapidly than the (real) log–Taylor expansion. Although the setup considered here differs significantly, our results are not in tension with theirs: they also obtain that, in regimes with a limited number of spectral parameters and frequency channels, the real log–Taylor expansion can indeed perform comparably to, or even slightly better than, the real moment expansion.

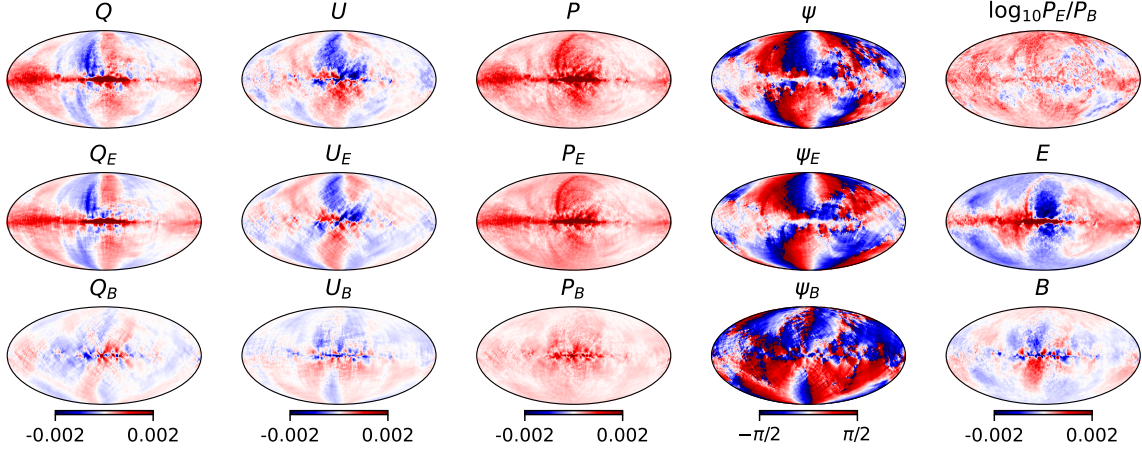


**Figure 10.** Similar to Fig. 5, but with PySM  $s5$  at 10 GHz.

## 4.2 More realistic sky model

We now turn to a more realistic synchrotron sky, using the  $s5$  model of PySM3 (Thorne et al. 2017; Zonca et al. 2021; Group et al. 2025, noted simply PySM hereafter), evaluated at a pivot frequency of 10 GHz. We first recall the morphology of the  $s5$  model in Sec. 4.2.1, with particular emphasis on the  $E/B$ -separated fields.

In this baseline model the polarization is, by construction, a rigid-angle power law in  $P$ : at each pixel,  $Q_\nu$ ,  $U_\nu$  and  $P_\nu$  share the same spectral index and exhibit no intrinsic curvature. In the language of Sec. 3, the sky is a pure power law in  $\underline{P}$  with  $\gamma = 0$  and all higher-order log–Taylor parameters vanishing. A log–Taylor fit around a pivot frequency should therefore return a single (real) spectral tilt and vanishing higher-order and angle-evolution parameters.

Any non-zero moments or curvature found in transformed fields must thus originate from the non-fully-local  $E/B$  operators rather than from the input SEDs. Because  $\underline{L}_E$  and  $\underline{L}_B$  are non-fully-local convolutions on the sphere, they mix structures with different morphology and orientation, exactly as discussed in Secs. 2 and 3.2. As a result,  $P_E$ ,  $P_B$  and  $S$  are not guaranteed to remain perfect power laws even when  $P$  is. This constitutes spectral complexity induced by the  $E/B$  transform itself, which we illustrate in Sec. 4.2.2.

We then demonstrate in Sec. 4.2.3 the complementarity of the two spectral expansions when only a limited number of frequency channels is available, before finally introducing in Sec. 4.2.4 a concrete diagnostic test to assess the performance of models built on  $\underline{P}_E$  and  $\underline{P}_B$  versus those built directly on  $\underline{P}$ .

### 4.2.1 Central frequency $E/B$ -separated maps (PySM $s5$ )

As a complement to the toy-model illustration of Sec. 4.1.1, we now show the morphology of the main polarization fields for the PySM  $s5$  model at 10 GHz.

Figure 10 displays full-sky maps of  $(Q, U)$ , the polarization amplitude  $P$ , the polarization angle  $\psi$ , and their  $E/B$ -separated counterparts, including  $P_E$ ,  $P_B$ ,  $\psi_E$ ,  $\psi_B$ , and the scalar fields  $E$  and  $B$ . While the Stokes maps encode the full information, their morphology is strongly dependent on the chosen coordinate frame and does not readily isolate physically distinct structures. In contrast, the  $E/B$ -separated spin-2 fields provide a direct and geometrically meaningful decomposition of the signal.

In particular, coherent large-scale features such as loops and fila-

mentary structures, which dominate the total polarized intensity  $P$ , are largely captured by  $P_E$  and are strongly suppressed in  $P_B$ . The  $E$ -family fields therefore appear well suited to isolate astrophysical loop-like structures and to address Galactic-science questions. Conversely, the  $B$ -family field, from which coherent  $E$ -mode structures have been filtered out, is of particular interest for tensor-to-scalar ratio searches.

The resulting “blobby”, turbulence-dominated morphology illustrated in row 3, column 3 of Fig. 10 may appear unfamiliar from a traditional CMB-analysis perspective. However, standard CMB analysis techniques can be applied directly in this  $r$ -contaminating foreground field, including component separation in local patches, mask construction based on thresholding a  $|\underline{P}_B|$ -based foreground tracer, and power-spectrum estimation from  $Q_B/U_B$ . Such an approach may offer improved optimality compared to analyses performed directly in  $(Q, U)$ ; quantifying this potential gain is left for future work.

The complementary nature of the two parity families is also clearly visible in the  $\log_{10}(P_E/P_B)$  ratio, which highlights regions dominated by one component or the other. This type of separation cannot be achieved at the level of  $Q$  and  $U$ , whose individual morphologies mix parity contributions and depend on the choice of reference frame. Once again, the  $\underline{P}_E/\underline{P}_B$  decomposition provides a clearer association between observed structures and their underlying physical origin.

This observation, already emphasized conceptually in previous sections, motivates a central goal of this work: constructing spectral analyses that operate on fields which are both geometrically well defined and capable of isolating distinct physical sources of polarized emission.

### 4.2.2 Spectral complexity induced by $E/B$ transform (PySM $s5$ )

We now turn to the spectral properties of the various polarization fields introduced above. The full-sky maps of the complex log–Taylor coefficients for the PySM  $s5$  model around 10 GHz are presented and briefly discussed in Appendix D (see Fig. 16), in direct analogy with the toy-model case. Here, we focus instead on a quantitative characterization of these fields through the distributions of their spectral parameters. Fig. 11 shows the corresponding pixel histograms, which we use to compare the spectral complexity induced by the  $E/B$  transform. The four panels display, respectively, the fitted spectral tilt  $\beta_X$  (top-left), the fitted curvature  $\gamma_X$  (top-right), the first derivative

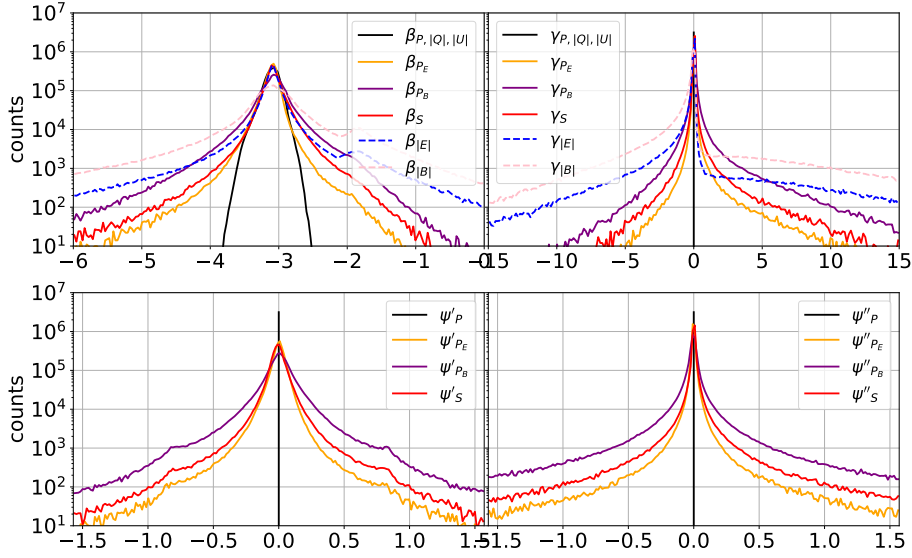


**Figure 11.** Pixel histograms (logarithmic y-axis) of fitted spectral parameters in the PySM *s5* model. Top-left: spectral tilt  $\beta_X$ . Top-right: curvature  $\gamma_X$ . Bottom-left: first angle derivative  $\psi'_X \equiv d\psi_X/ds$ . Bottom-right: second angle derivative  $\psi''_X \equiv d^2\psi_X/ds^2$ . Curves are shown for  $X \in \{P, P_E, P_B, S, |E|, |B|\}$ ; the  $P$  curve also overlaps the corresponding distributions for  $|Q|$  and  $|U|$  in this model. The vertical line marks zero in the  $\gamma$ ,  $\psi'$  and  $\psi''$  panels.

(wrt.  $s$ ) of the polarization angle  $\psi'_X$  (bottom-left), and the second derivative  $\psi''_X$  (bottom-right).

The curves correspond to  $X \in \{P, P_E, P_B, S, |E|, |B|\}$ , with the  $P$  curve also coinciding with the histograms obtained from  $|Q|$  and  $|U|$  in this model. In the  $\gamma$ ,  $\psi'$  and  $\psi''$  panels, the vertical line indicates zero as expected for  $s5$ . The  $\beta_P$  distribution is peaked around its  $s5$  fiducial value, while  $\beta_{P_E}$ ,  $\beta_{P_B}$  and  $\beta_S$  exhibit wider tails. The broadest  $\beta$  distributions are those of  $|E|$  and  $|B|$ . The same hierarchy appears in the curvature panel:  $\gamma_P$  is narrowly concentrated at  $\gamma = 0$ , whereas  $\gamma_{P_E}$ ,  $\gamma_{P_B}$  and  $\gamma_S$  extend to non-zero values, and  $|E|$  and especially  $|B|$  show the widest tails. Finally,  $\psi'_X$  and  $\psi''_X$  are both distributed symmetrically around zero; their dispersions are smallest for  $P_E$ , larger for  $S$ , and largest for  $P_B$ .

The interpretation is immediate once placed in the context of the previous sections. Because  $s5$  enforces a rigid-angle power law for  $\underline{P}$ , the delta-like distributions for  $(\gamma_P, \psi'_P, \psi''_P)$  simply reflect the input assumption:  $P$  (and likewise  $|Q|$  and  $|U|$ ) is spectrally a rigid-angle power-law. The broadening observed for  $P_E$ ,  $P_B$  and  $S$  must therefore be induced by the map-space operators used to construct these fields. This is exactly the mechanism anticipated in our discussion of (partial) non-locality: the  $E/B$  projection reorganizes the same underlying morphology into parity channels through non-fully-local kernels, and the derived fields inherit effective spatially varying tilts, curvatures, and angle-evolution parameters even when the underlying SED is uniform.

Two additional conclusions follow from Fig. 11. First,  $|E|$  and  $|B|$  exhibit the strongest induced distortions (widest wings in both  $\beta$  and  $\gamma$ ), *i.e.* they suffer from *more* apparent spectral complexity than  $S$  and, a fortiori, than the spin-preserving amplitudes  $P_E$  and  $P_B$ . In this sense, the fields built from the standard scalar  $E$  and  $B$  maps are the least spectrally stable objects to analyse in map space, while  $P_E$  and  $P_B$  retain the most controlled behaviour among the non-fully-local constructed quantities.

Second, and crucially for practical use, these conclusions are insensitive to the truncation scale of the  $E/B$  transform. Although not shown here, we have repeated the analysis for  $\ell_{\max} = 95$  and  $\ell_{\max} = 11$  (instead of  $\ell_{\max} = 1535$ ) and found essentially unchanged

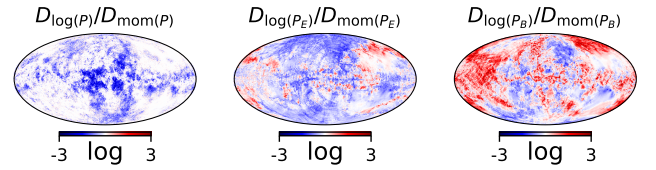


**Figure 12.** Same as Fig. 9 in the case of the PySM *s5* model.

distributions. If the distortions were dominated by the finite support of the real-space kernels (“effective beam” or kernel-truncation effects; see Rotti & Huffenberger 2019), one would expect them to widen when increasing  $\ell_{\max}$ . This is not observed: the non-fully-locality associated with the kernel width is subdominant compared to the intrinsic geometric differences between the  $E$ - and  $B$ -like projections of the polarization tensor. In other words, the extra spectral complexity of  $P_E$ ,  $P_B$ ,  $S$ , and especially of  $|E|$  and  $|B|$ , is mainly a consequence of the  $E/B$  geometry in map space, not a technical artefact of the numerical implementation.

#### 4.2.3 Performance with a finite number of channels (PySM *s5*)

We now repeat, on the PySM *s5* synchrotron model, the same three-channel reconstruction test introduced for the toy model in Sec. 4. We evaluate the “truth” maps at  $\nu = \{5, 10, 15\}$  GHz with pivot  $\nu_0 = 10$  GHz, and for each complex field  $\underline{X} \in \{P, P_E, P_B\}$  we build two second-order reconstructions: (i) a truncated complex log-Taylor model and (ii) a truncated complex moment model (each retaining three complex spectral parameters per pixel; cf. Eqs. 12 and 15). The reconstruction quality is quantified by the complex generalization of the diagnostic  $D_{\underline{X}}$  defined in Eq. 93. As in the toy-model case, we compare the two parametrizations through the ratio of errors,  $\log_{10}[D_{\log(X)}/D_{\text{mom}(X)}]$ , shown in Fig. 12. Blue regions correspond to  $D_{\log} < D_{\text{mom}}$  (log-Taylor performs better), while red regions indicate the opposite.

The three panels of Fig. 12 display distinct behaviours. For the

total field  $\underline{P}$  (left), the map is predominantly blue-to-white, with comparatively weak spatial contrast. For  $\underline{P}_E$  (middle), blue regions still cover a large fraction of the sky, but extended red patches appear. For  $\underline{P}_B$  (right), the pattern reverses: red regions dominate, with only a limited set of blue structures.

These trends can be interpreted in direct continuity with the toy-model discussion. In the s5 model, the underlying emission is constructed to be spectrally rigid in  $\underline{P}$  (and hence in  $Q$  and  $U$ ): the true frequency dependence is close to a single power law with a fixed polarization angle. It is therefore unsurprising that, for  $P$ , a clear preference is seen for the log-Taylor expansion (blue).

The situation becomes more instructive once the non-fully-local  $E/B$  operators are applied. As established earlier (Sec. 2 and illustrated in Sec. 4.2), even a spectrally simple  $\underline{P}$  generically acquires effective SED distortions in  $\underline{P}_E$  and  $\underline{P}_B$  because the map-space projections mix morphology in a non-fully-local way. Fig. 12 shows that these induced distortions are captured with different success by the two low-order parametrizations: the log-Taylor truncation remains preferable over large areas for  $P_E$ , while the moment truncation becomes more favourable for  $P_B$  over much of the sky. Compared to the toy model, where the log-Taylor description tended to dominate more uniformly, the s5 case therefore highlights a more field-dependent competition once realistic full-sky morphology and  $E/B$ -induced distortions are present.

Overall, this test confirms that (i) the ranking between parametrizations is not purely formal but can depend on which derived field is modelled, and (ii) for realistic skies the  $E$ - and  $B$ -projected fields need not share the same “best” low-order spectral description, even when the underlying  $\underline{P}$  is close to a rigid power law. This motivates carrying both descriptions forward as practical tools, and, crucially, testing them directly on the data in any three-band analysis, rather than assuming *a priori* that one truncation will be uniformly optimal on all parity channels.

#### 4.2.4 Distinguishing between a power law in $P$ and in $(P_E, P_B)$

The previous paragraphs addressed a first, “within-field” question: given a fixed field  $\underline{X} \in \{\underline{P}, \underline{P}_E, \underline{P}_B\}$  and only three frequency channels, which low-order spectral parametrization (complex log-Taylor or complex moments) most accurately transports that *same* field across frequency? We now turn to a complementary, and more operational, question that matters directly for foreground extrapolation: *in which field should one model the signal in the first place?*

Indeed, Secs. 2 and 3 established that the  $E/B$  projections are not fully local and can redistribute spectral complexity even when the underlying  $\underline{P}$  is spectrally simple. This was illustrated explicitly in the toy model (Sec. 4.1.4) and in the PySM s5 case (Sec. 4.2.3): in a model that is a rigid-angle power law in  $\underline{P}$ , the derived fields  $\underline{P}_E$  and  $\underline{P}_B$  generally acquire effective spectral distortions. Conversely, one may consider the opposite limiting construction, in which  $\underline{P}_E$  and  $\underline{P}_B$  are each simple power laws, at the expense of allowing  $\underline{P}$  to become spectrally complex. These two extremes bracket plausible behaviours of real data, which are expected to lie somewhere in between.

This motivates studying two natural limiting assumptions:

(i) *Power law in  $P$  (rigid angle)*. One assumes a single SED per pixel for  $Q$ ,  $U$  and  $P$ ; the polarization angle is independent of frequency, and any  $E/B$  asymmetry arises purely from geometry and non-fully-local projection.

(ii) *Power laws in  $(P_E, P_B)$  (non-rigid angle)*. One assumes independent SEDs for  $P_E$  and  $P_B$ , allowing the polarization angle of

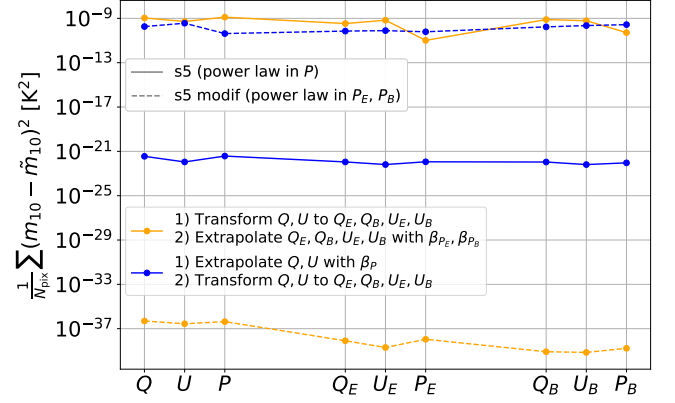


**Figure 13.** Mean-squared prediction error in the intermediate-frequency channel (10 GHz) for  $Q, U, P, Q_E, U_E, P_E, Q_B, U_B, P_B$  when extrapolating from two surrounding frequencies under the two hypotheses. Blue curves: assuming a single power law in  $P$  (Hypothesis P). Orange curves: assuming independent power laws in  $P_E$  and  $P_B$  (Hypothesis EB). Solid lines: true sky is the standard s5 model (power law in  $P$ ). Dashed lines: true sky is the modified model with power laws in  $(P_E, P_B)$ .

the total field to vary with frequency through a change in the relative weight of  $E$ - and  $B$ -like patterns (as in Secs. 3.2 and 3.6).

A very practical question is therefore: *can we tell, from three noiseless frequency channels, which of these two hypotheses provides the more faithful effective description of a given sky realization?*

To address this, we construct and compare two extreme PySM-based models:

**The standard s5 model**, in which  $Q, U$  and  $P$  share the same power-law SED at each pixel (“power law in  $P$ ”). As in the previous subsection, any spectral complexity in  $P_E, P_B$  or  $S$  is induced by the  $E/B$  transform.

**A modified s5-like model**, in which we impose instead that  $P_E$  and  $P_B$  follow independent power laws, with indices  $\beta_{P_E}$  and  $\beta_{P_B}$ , while allowing  $P$  to become spectrally complex when recombining  $E$  and  $B$ . This represents the opposite extreme: “power laws in  $(P_E, P_B)$ ” with non-trivial frequency evolution in  $P$ .

In both cases the morphology at the pivot frequency is kept identical, so that differences arise only from how the sky is propagated in frequency. We typically expect real data to lie in between these two extremes.

We then perform a simple prediction experiment using three noiseless frequency channels: two widely separated frequencies,  $\nu_{\text{low}} = 5$  GHz and  $\nu_{\text{high}} = 15$  GHz, and one intermediate channel  $\nu_{\text{mid}} = 10$  GHz. For each of the two sky models, we compare two extrapolation schemes:

**Hypothesis P (power law in  $P$ )**. We fit, pixel by pixel, a single spectral index  $\beta_P$  from the low and high frequencies (equivalently from  $Q$  and  $U$  or from  $P$ ), extrapolate  $Q$  and  $U$  to  $\nu_{\text{mid}}$  under this power-law assumption, and then apply the  $E/B$  transform to obtain  $P_E$  and  $P_B$  at the intermediate frequency.

**Hypothesis EB (power laws in  $(P_E, P_B)$ )**. We first transform each frequency map to  $P_E$  and  $P_B$ , then fit independent indices  $\beta_{P_E}$  and  $\beta_{P_B}$  from the low and high frequencies, extrapolate  $P_E$  and  $P_B$  to  $\nu_{\text{mid}}$ , and finally recombine back to  $Q$  and  $U$  at the intermediate channel.

For each hypothesis and each sky model (four cases in total) we

compute the mean-squared prediction error in the intermediate band for several fields:  $Q$ ,  $U$ ,  $P$ ,  $Q_E$ ,  $U_E$ ,  $P_E$ ,  $Q_B$ ,  $U_B$  and  $P_B$ <sup>7</sup>.

The results, summarized in Fig. 13, are clear. When the true sky follows a power law in  $P$  (solid curves), Hypothesis P yields significantly smaller errors for all tested quantities. Extrapolating in  $(P_E, P_B)$  under Hypothesis EB amounts to fitting the wrong spectral model and degrades the predictions. Conversely, when the true sky follows power laws in  $(P_E, P_B)$  (dashed curves), the situation reverses: Hypothesis EB systematically outperforms Hypothesis P. In this case, enforcing a rigid-angle SED in  $P$  is the wrong approximation.

Even with only three noiseless channels, the two hypotheses are therefore easily distinguishable: the data themselves select the spectral description that is closer to the truth. Real observations will of course include noise, bandpass uncertainties, and additional systematics, but the basic diagnostic remains valid. By comparing prediction errors under different parametric assumptions, one can test whether the sky behaves more like a power law in  $P$  or more like power laws in  $(P_E, P_B)$ . We emphasize that the latter case should not be interpreted literally as the expectation of exact power laws in  $P_E$  and  $P_B$ ; rather, it represents an intentionally idealized opposite extreme to the rigid power-law-in- $P$  scenario, introduced here solely for diagnostic and interpretative purposes.

This has direct implications for CMB component separation and related applications (*e.g.*, clustering, masking, or local template fitting). The choice of working hypothesis (whether to extrapolate a single SED in  $P$  or independent SEDs in  $P_E$  and  $P_B$ ) controls how spectral complexity is modelled and where it is allowed to reside (in  $P$  or in its  $E/B$  components). The simple experiment above shows that, in an idealized setting, three frequency channels already carry enough information to discriminate between these limiting cases. Applying analogous diagnostics to real multi-frequency data will therefore be a crucial step in deciding which modelling strategy is actually supported by the data.

## 5 SUMMARY AND CONCLUSIONS

In this work we have developed a unified, map-space framework to describe the frequency dependence of polarized synchrotron emission, with particular emphasis on field representations that preserve the spin-2 nature of the signal. Our motivation is practical: map-space  $E/B$  separation is attractive for both Galactic studies and CMB analysis because it organizes the polarization morphology by parity, isolating  $B$ -family structures that are the actual potential contaminant in the search primordial tensor modes. This naturally suggests performing spectral modelling in  $E/B$ -separated fields rather than in  $(Q, U)$  or in the total complex polarization  $\underline{P} = Q + iU$ . The central difficulty, however, is that the map-space  $E/B$  transform is non-fully-local, so it can induce additional apparent spectral complexity in the projected fields even when the underlying sky is spectrally simple in  $\underline{P}$ . This point is crucial in practice for both CMB and Galactic sciences, because increased spectral complexity translates into more spectral parameters to fit, can prevent stable foreground extrapolation or parametric component separation when the number of available

frequency channels is limited, and leads to morphologies that are not conserved across frequencies.

By working with  $\underline{P}$  and its spin-preserving  $E$ - and  $B$ -family projections  $\underline{P}_E$  and  $\underline{P}_B$ , we introduced complex log-Taylor and moment expansions that treat amplitude and polarization angle on the same footing. We show that the two parametrizations are mathematically equivalent, but conceptually complementary: log-Taylor coefficients provide an intuitive generalization of the familiar “amplitude-tilt-curvature” description used in the literature, while moments are linear in the field and therefore transform trivially under any linear operator. In this language, the closure relation between  $\underline{P}$ ,  $\underline{P}_E$  and  $\underline{P}_B$  extends to all spectral orders, and we obtained simple transformation rules for moments and complex spectral parameters under  $E/B$  projection.

Building on this formalism, we derived analytic predictions for the first spectral moments of several key synchrotron mechanisms: spatial variations of the spectral index, line-of-sight superposition of components with different indices and angles, intrinsic curvature, synchrotron ageing, and internal and external Faraday rotation and depolarization. These results clarify which effects generate amplitude-only evolution and which also drive frequency-dependent changes of the polarization angle and thus  $E \leftrightarrow B$  mixing. We then validated the full chain of formulae on a controlled toy model, showing that the predicted moments and complex log-Taylor coefficients accurately reproduce those fitted from maps. We further quantified how map-space  $E/B$  separation redistributes spectral complexity across field choices: the real scalar fields  $|E|$  and  $|B|$  are systematically the most spectrally complex, while the complex scalar  $\underline{S} = E + iB$  is less affected but does not provide a directly interpretable amplitude and angle. By contrast, the spin-2 fields  $\underline{P}_E$  and  $\underline{P}_B$  exhibit only moderate (though non-negligible) induced distortions while retaining a clear geometric meaning. A more realistic PySM synchrotron sky confirmed these conclusions: even when the input model is a pure power law in  $P$ , the non-fully-local  $E/B$  transform induces non-negligible spectral distortions in  $\underline{P}_E$ ,  $\underline{P}_B$  and  $\underline{S}$ , and much larger distortions in  $|E|$  and  $|B|$ , with little dependence on the multipole cut of the transform. When only three frequency channels are available, we further find that low-order log-Taylor and moment truncations can both provide useful and complementary models. Finally, by contrasting a standard PySM model (power law in  $P$ ) with a modified model (power laws in  $P_E$  and  $P_B$ ), we showed that three frequency channels already suffice to discriminate between a sky whose spectral properties are effectively captured by a single power law in  $P$  and one that is better described as independent power laws in  $(P_E, P_B)$ .

These results have direct implications for both Galactic science and CMB analysis, and they motivate clear practical recommendations. We recommend performing  $E/B$  separation in map space and modelling frequency dependence directly in the spin-preserving fields  $\underline{P}_E$  and  $\underline{P}_B$ , rather than at the level of  $(Q, U)$  or  $P$  (which do not isolate parity families) or in scalar combinations such as  $|E|$ ,  $|B|$  or  $\underline{S}$  (which tend to be intrinsically more spectrally complex for  $|E|$ ,  $|B|$  or less directly interpretable for  $\underline{S}$ ). In this approach, complex moments or complex log-Taylor parameters provide compact, physically informative descriptions that simultaneously capture amplitude evolution and frequency-dependent polarization-angle changes. For Galactic studies,  $\underline{P}_E$  and  $\underline{P}_B$  offer diagnostics of how distinct mechanisms (coherent fields and loops that primarily generate  $E$ -like radial patterns, turbulence producing mixed  $E$  and  $B$  structure, ageing, Faraday effects, and line-of-sight mixing) feed into  $E$ - and  $B$ -like morphology while remaining directly interpretable in map space. For CMB experiments, where  $B$ -modes are the primary target and

<sup>7</sup> This test, which we plan to apply to real data, will of course require a more sophisticated statistical treatment in order to provide a robust assessment of the preferred model using model-comparison techniques. Here, we deliberately keep the method simple to illustrate the principle and leave room for more advanced treatments.

$E/B$  separation is ubiquitous, the same strategy supports foreground spectral modelling in a representation that is better aligned with the map-level quantities relevant to  $r$  and avoids unnecessary induced complexity.

Beyond the present work, and looking ahead in this direction, working directly with  $\underline{P}_B$  in the context of CMB  $r$  inference is straightforward. Within this field one can carry out the usual map-space operations: extrapolate foreground templates across frequency; perform component separation and define local patches or clusters consistently in the same representation (with parametric, see *e.g.* Stompor et al. 2009, or agnostic methods, see *e.g.* Bennett et al. 2003; Delabrouille et al. 2009); construct map-space estimators of  $r$ , including pixel-based likelihoods (see *e.g.* Eriksen et al. 2007); and estimate  $C_\ell^{BB}$  with standard techniques, such as the quasi-maximum-likelihood method (see *e.g.* Tegmark 1997) directly from maps or pseudo- $C_\ell$  estimators (see *e.g.* Hivon et al. 2002). In this approach, masks can naturally be constructed by thresholding a foreground-tracer map built from  $|\underline{P}_B|$  amplitude, rather than in  $P$ . Based on the results presented in this work, one can already develop an intuition for the potential gains of such a strategy (in particular, pixels are no longer contaminated by non- $B$  variance arising from  $E$ -like foreground structures that are readily generated by astrophysical sources like polarized synchrotron loops). Quantifying these gains for each application and for specific data sets is deferred to subsequent works in this series.

In particular, we will follow our own recommendations in forthcoming works on synchrotron polarization using new  $C$ -BASS (see Jones et al. 2018; Taylor et al. 2026) data complemented by  $S$ -PASS (see Krachmalnicoff et al. 2018; Carretti et al. 2019),  $WMAP$  (see Bennett et al. 2013) and  $Planck$  observations (see Aghanim et al. 2020). These recommendations will be equally important for upcoming CMB analyses using data from, for example, the *Simons Observatory* (see Abitbol et al. 2019) and *LiteBIRD* (see Allys et al. 2023) and including foreground extrapolation, mask and cluster construction, component separation, or any pixel-space estimators.

## ACKNOWLEDGEMENTS

We thank Alessandro Carones, Ishaque Khan and the *RadioForegroundsPlus* collaboration, as well as members of the BIPAC and CMB-OX in Oxford, for useful comments and discussions.

We acknowledge support from the Horizon Europe Project RadioForegroundsPlus HORIZON-CL4-2023-SPACE-01, GA 101135036, which is supported in the UK by UKRI grant number 10101603. We acknowledge partial support by the Italian Space Agency LiteBIRD Project (ASI Grants No. 2020-9-HH.0 and 2016-24-H.1-2018), as well as the InDark and LiteBIRD Initiative of the National Institute for Nuclear Physics, and Project SPACE-IT-UP by the Italian Space Agency and Ministry of University and Research, Contract Number 2024-5-E.0 and the CMB-Inflate project funded by the European Union's Horizon 2020 Research and Innovation Staff Exchange under the Marie Skłodowska-Curie grant agreement No 101007633.

We made extensive use of the *numpy* (van der Walt et al. 2011), *astropy* (Price-Whelan et al. 2018), *healpy* (Zonca et al. 2019) and *matplotlib* (Hunter 2007) python packages, as well as the *HEALPix* package (Górski et al. 2005). The AI tool ChatGPT 5.2, accessed through the *Oxford University ChatGPT Edu Workspace*, was used solely for language editing and stylistic refinement. We, human authors, take full responsibility for the content of the manuscript.

## DATA AVAILABILITY

The (mock) data that support the figures and plots of this paper are available from the corresponding author upon request.

## REFERENCES

- Abitbol M. H., et al., 2019, *Bull. Am. Astron. Soc.*, 51, 147  
 Ackermann M., et al., 2012, *Astrophys. J.*, 750, 3  
 Adak D., et al., 2025, arXiv preprint  
 Ade P. A. R., et al., 2016, *Astrophys. J.*, 825, 66  
 Aghanim N., et al., 2020, *Astron. Astrophys.*, 641, A1  
 Akrami Y., et al., 2020, *Astron. Astrophys.*, 641, A4  
 Allys E., et al., 2023, *PTEP*, 2023, 042F01  
 Azzoni S., Abitbol M. H., Alonso D., Gough A., Katayama N., Matsumura T., 2021, *JCAP*, 05, 047  
 Azzoni S., Alonso D., Abitbol M. H., Errard J., Krachmalnicoff N., 2023, *JCAP*, 03, 035  
 Bennett C., et al., 2003, *Astrophys. J. Suppl.*, 148, 97  
 Bennett C. L., et al., 2013, *Astrophys. J. Suppl.*, 208, 20  
 Burn B. J., 1966, *Monthly Notices of the Royal Astronomical Society*, 133, 67  
 Carones A., Remazeilles M., 2024, *JCAP*, 06, 018  
 Carretti E., et al., 2019, *Mon. Not. Roy. Astron. Soc.*, 489, 2330  
 Chluba J., Hill J. C., Abitbol M. H., 2017, *Mon. Not. Roy. Astron. Soc.*, 472, 1195  
 Delabrouille J., Cardoso J. F., Jeune M. L., Betoule M., Fay G., Guilloux F., 2009, *Astron. Astrophys.*, 493, 835  
 Eriksen H. K., et al., 2007, *Astrophys. J.*, 656, 641  
 Galloway M., et al., 2023, *Astron. Astrophys.*, 675, A3  
 Górski K. M., Hivon E., Banday A. J., Wandelt B. D., Hansen F. K., Reinecke M., Bartelman M., 2005, *Astrophys. J.*, 622, 759  
 Group T. P.-E. G. S., et al., 2025, *The Astrophysical Journal*, 991, 23  
 Guillet V., Vacher L., Aumont J., Boulanger F., Ritacco A., Delouis J.-M., Bracco A., 2025, arXiv preprint  
 Hivon E., Gorski K. M., Netterfield C. B., Crill B. P., Prunet S., Hansen F., 2002, *Astrophys. J.*, 567, 2  
 Hu W., White M. J., 1997, *New Astron.*, 2, 323  
 Hunter J. D., 2007, *Comput. Sci. Eng.*, 9, 90  
 Ichiki K., Kanai H., Katayama N., Komatsu E., 2019, *PTEP*, 2019, 033E01  
 Jones M. E., et al., 2018, *Mon. Not. Roy. Astron. Soc.*, 480, 3224  
 Kamionkowski M., Kovetz E. D., 2016, *Ann. Rev. Astron. Astrophys.*, 54, 227  
 Kamionkowski M., Kosowsky A., Stebbins A., 1997, *Phys. Rev. D*, 55, 7368  
 Krachmalnicoff N., et al., 2018, *Astron. Astrophys.*, 618, A166  
 Liu H., 2018, *Astron. Astrophys.*, 617, A90  
 Liu H., Creswell J., Naselsky P., 2018, *JCAP*, 05, 059  
 Liu H., Creswell J., Tsai C.-W., Naselsky P., 2023, *JCAP*, 11, 025  
 Liu Y., et al., 2025, *JCAP*, 11, 024  
 Mangilli A., Aumont J., Rotti A., Boulanger F., Chluba J., Ghosh T., Montier L., 2021, *Astron. Astrophys.*, 647, A52  
 Martire F. A., Banday A. J., Martínez-González E., Barreiro R. B., 2023, *JCAP*, 04, 049  
 Murgia M., Fanti C., Fanti R., Gregorini L., Klein U., Mack K.-H., Vigotti M., 1999, *A&A*, 345, 769  
 Pacholczyk A. G., 1970, *Radio astrophysics. Nonthermal processes in galactic and extragalactic sources.* W. H. Freeman and Company, San Francisco  
 Price-Whelan A. M., et al., 2018, *Astron. J.*, 156, 123  
 Price D. J., Bate M. R., Dobbs C. L., 2009, *Rev. Mex. Astron. Astrof. Ser. Conf.*, 36, 128  
 Remazeilles M., Rotti A., Chluba J., 2021, *Mon. Not. Roy. Astron. Soc.*, 503, 2478  
 Rizzieri A., Leloup C., Errard J., Poletti D., 2025, arXiv preprint  
 Rotti A., Huppenberger K., 2019, *JCAP*, 01, 045  
 Rybicki G. B., 2004, *Radiative Processes in Astrophysics.* Wiley-VCH, doi:10.1002/9783527618170  
 Seljak U., Zaldarriaga M., 1997, *Phys. Rev. Lett.*, 78, 2054

- Sokoloff D. D., Bykov A. A., Shukurov A., Berkhuijsen E. M., Beck R., Poezd A. D., 1998, *Monthly Notices of the Royal Astronomical Society*, 299, 189
- Stompor R., Leach S. M., Stivoli F., Baccigalupi C., 2009, *Mon. Not. Roy. Astron. Soc.*, 392, 216
- Taylor A. C., et al., 2026, In preparation.
- Tegmark M., 1997, *Phys. Rev. D*, 55, 5895
- Thorne B., Dunkley J., Alonso D., Næss S., 2017, *Monthly Notices of the Royal Astronomical Society*, 469, 2821–2833
- Vacher L., Aumont J., Montier L., Azzoni S., Boulanger F., Remazeilles M., 2022, *Astron. Astrophys.*, 660, A111
- Vacher L., Chluba J., Aumont J., Rotti A., Montier L., 2023a, *Astron. Astrophys.*, 669, A5
- Vacher L., Aumont J., Boulanger F., Montier L., Guillet V., Ritacco A., Chluba J., 2023b, *Astron. Astrophys.*, 672, A146
- Vacher L., Carones A., Aumont J., Chluba J., Krachmalnicoff N., Ranucci C., Remazeilles M., Rizzieri A., 2025, *Astron. Astrophys.*, 697, A212
- Waelkens A. H., Schekochihin A. A., Enßlin T. A., 2009, *Monthly Notices of the Royal Astronomical Society*, 398, 1970
- Wolz K., et al., 2024, *Astron. Astrophys.*, 686, A16
- Zaldarriaga M., Seljak U., 1997, *Phys. Rev. D*, 55, 1830
- Zonca A., Singer L., Lenz D., Reinecke M., Rosset C., Hivon E., Gorski K., 2019, *Journal of Open Source Software*, 4, 1298
- Zonca A., Thorne B., Krachmalnicoff N., Borrill J., 2021, *Journal of Open Source Software*, 6, 3783
- de la Hoz E., et al., 2023, *Mon. Not. Roy. Astron. Soc.*, 519, 3504
- van der Walt S., Colbert S. C., Varoquaux G., 2011, *Comput. Sci. Eng.*, 13, 22

## APPENDIX A: WHY $\mathcal{P}_{ab}^{(E)}$ AND $\mathcal{P}_{ab}^{(B)}$ ARE SPIN-2 TENSORS

We show below that the  $E/B$  parts of the linear polarization inherit the same spin-2 transformation law as the full polarization tensor  $\mathcal{P}_{ab}$ .

The linear polarization at a point on the sphere can be represented by the symmetric, trace-free tensor, written in the local orthonormal tangent basis  $(\hat{e}_\theta, \hat{e}_\phi)$  as Eq. 1. A local rotation of this tangent basis by angle  $\alpha$ ,  $(\hat{e}_\theta, \hat{e}_\phi) \mapsto (\hat{e}'_\theta, \hat{e}'_\phi) = R(\alpha)(\hat{e}_\theta, \hat{e}_\phi)$  changes the Stokes parameters according to

$$(Q \pm iU)'(\mathbf{n}) = e^{\mp 2i\alpha} (Q \pm iU)(\mathbf{n}). \quad (\text{A1})$$

This is the defining property of a spin- $\mp 2$  field on the sphere. Equivalently,  $\mathcal{P}_{ab}$  transforms under the action of the rotation on its tensor indices as a rank-2 symmetric traceless object.

Because  $Q \pm iU$  are spin- $\mp 2$  fields they admit the spin-weighted harmonic expansion

$$(Q \pm iU)(\mathbf{n}) = \sum_{\ell m} a_{\ell m}^{\pm 2} {}_2Y_{\ell m}(\mathbf{n}), \quad (\text{A2})$$

where  ${}_2Y_{\ell m}$  denotes the spin-2 spherical harmonics. The standard  $E$  and  $B$  harmonic coefficients are defined by the linear combinations,

$$a_{\ell m}^E = -\frac{1}{2}(a_{\ell m}^2 + a_{\ell m}^{-2}) \quad \text{and} \quad a_{\ell m}^B = \frac{i}{2}(a_{\ell m}^2 - a_{\ell m}^{-2}). \quad (\text{A3})$$

The inverse transform reconstructs the  $E$  and  $B$  contributions to the spin-2 fields:

$$(Q_E \pm iU_E)(\mathbf{n}) = \sum_{\ell m} a_{\ell m}^E {}_2Y_{\ell m}(\mathbf{n}) \quad \text{and} \quad (\text{A4})$$

$$(Q_B \pm iU_B)(\mathbf{n}) = \sum_{\ell m} (\mp i) a_{\ell m}^B {}_2Y_{\ell m}(\mathbf{n}). \quad (\text{A5})$$

From there, we easily verify that  $Q \pm iU = (Q_E \pm iU_E) + (Q_B \pm iU_B)$ .

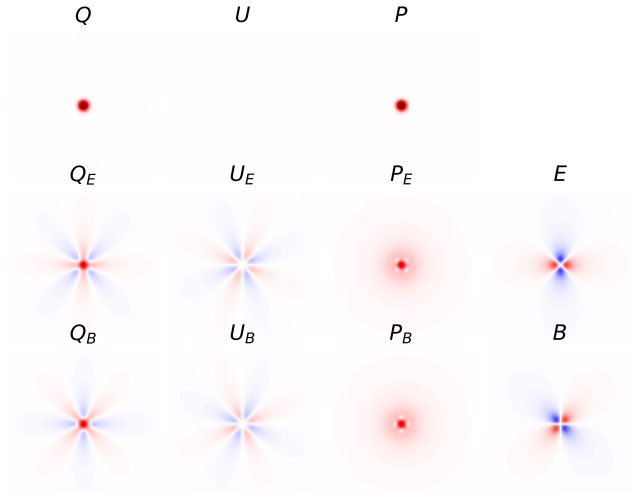


**Figure 14.** Transformation of a two-dimensional positive Gaussian feature in  $Q$  into the various  $E$ - and  $B$ -mode fields. The panels show, from left to right, the input Stokes fields  $(Q, U, P, \psi)$  followed by the derived  $E$ -family fields  $(Q_E, U_E, P_E, E)$  and the  $B$ -family fields  $(Q_B, U_B, P_B, B)$ . The color maps is the same for all panels (blue = negative, red = positive).

$iU_B$ ). Furthermore, under a local rotation by  $\alpha$  the spin-2 weighted harmonics transform as

$${}_2Y'_{\ell m}(\mathbf{n}) = e^{-2i\alpha} {}_2Y_{\ell m}(\mathbf{n}). \quad (\text{A6})$$

Therefore each harmonic term in the sums for  $Q_E \pm iU_E$  and  $Q_B \pm iU_B$  acquires the same phase factor  $e^{\mp 2i\alpha}$  as the corresponding term in the full field. Concretely, using the inverse transforms above,

$$(Q_E \pm iU_E)'(\mathbf{n}) = \sum_{\ell m} a_{\ell m}^E {}_2Y'_{\ell m}(\mathbf{n}) \quad (\text{A7})$$

$$= e^{\mp 2i\alpha} \sum_{\ell m} a_{\ell m}^E {}_2Y_{\ell m}(\mathbf{n}) \quad (\text{A8})$$

$$= e^{\mp 2i\alpha} (Q_E \pm iU_E)(\mathbf{n}), \quad (\text{A9})$$

and similarly  $Q_B \pm iU_B$ .

We then define the  $E$  and  $B$  polarization tensors as in Eq. 1 but replacing  $(Q, U)$  by  $(Q_E, U_E)$  and  $(Q_B, U_B)$  respectively. Since  $Q_E \pm iU_E$  and  $Q_B \pm iU_B$  each satisfy the spin-2 transformation law  $(Q \pm iU)' = e^{\mp 2i\alpha} (Q \pm iU)$ , the tensors  $\mathcal{P}_{ab}^{(E)}$  and  $\mathcal{P}_{ab}^{(B)}$  transform in the same way under local rotations of the tangent frame as the full  $\mathcal{P}_{ab}$ . Therefore each is a spin-2 (symmetric, traceless) tensor field on the sphere.

## APPENDIX B: CONVOLUTION KERNELS

The real-space kernels that relate  $(Q, U)$  to the  $E$ - and  $B$ -family fields  $(Q_E, U_E)$  and  $(Q_B, U_B)$  are derived in Rotti & Huffenberger (2019). We denote by  $\mathcal{K}_I$  and  $\mathcal{K}_D$  the two radial kernels introduced in their Eq. (3.23) (under the notation  ${}_I f$  and  ${}_D f$ ).

On a discrete pixelization, let indices  $p$  and  $q$  correspond to sky directions  $\mathbf{n}$  and  $\mathbf{n}'$ , respectively, and let  $\alpha_{qp}, \beta_{qp}, \gamma_{qp}$  be the Euler angles of the rotation mapping  $\mathbf{n}' \rightarrow \mathbf{n}$  in the  $\text{SO}(3)$  convention of Rotti & Huffenberger (2019). Then the complex  $E/B$  family fields in

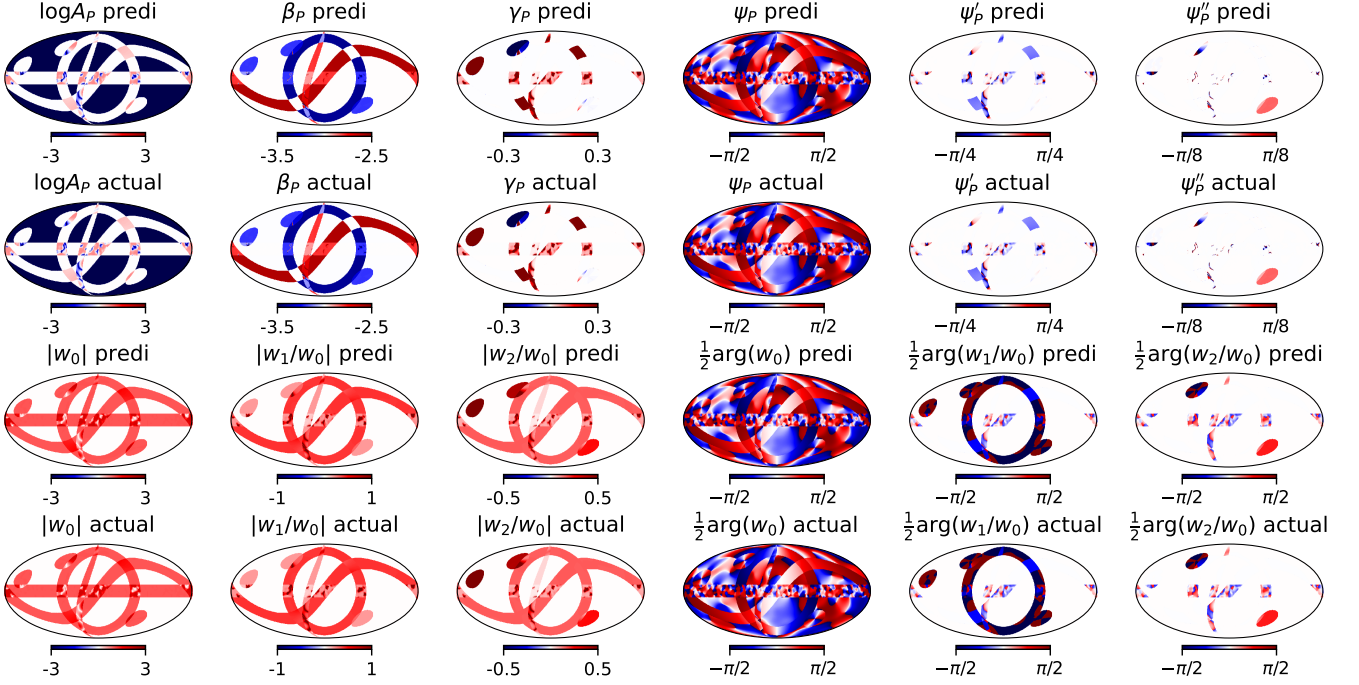


**Figure 15.** Full-sky Mollweide maps of spectral quantities for the toy-model total polarization field  $P$ . From left to right, columns show  $\log A_P$ ,  $\beta_P$ ,  $\gamma_P$ ,  $\psi_P$ ,  $\psi'_P$  and  $\psi''_P$  (first and second columns of panels) and, in the lower part,  $|w_0|$ ,  $|w_1/w_0|$ ,  $|w_2/w_0|$ ,  $\frac{1}{2} \arg(w_0)$ ,  $\frac{1}{2} \arg(w_1/w_0)$  and  $\frac{1}{2} \arg(w_2/w_0)$ . The first and third rows display the quantities predicted from the analytic relations of Sec. 3, while the second and fourth rows display the corresponding quantities obtained by fitting a complex log–Taylor expansion to the three toy-model frequency maps. Each panel includes its own colour bar, with units matching the corresponding parameter.

pixel  $p$  can be written as

$$\underline{P}_{E,p} = \sum_q \Delta\Omega \left[ \mathcal{K}_I(\beta_{qp}) e^{-2i(\alpha_{qp} + \gamma_{qp})} \underline{P}_q + \mathcal{K}_D(\beta_{qp}) e^{2i(\alpha_{qp} - \gamma_{qp})} \underline{P}_q^* \right], \quad (\text{B1})$$

$$\underline{P}_{B,p} = \sum_q \Delta\Omega \left[ \mathcal{K}_I(\beta_{qp}) e^{-2i(\alpha_{qp} + \gamma_{qp})} \underline{P}_q - \mathcal{K}_D(\beta_{qp}) e^{2i(\alpha_{qp} - \gamma_{qp})} \underline{P}_q^* \right], \quad (\text{B2})$$

where  $\Delta\Omega$  is the pixel area and  $\mathcal{K}_I$  and  $\mathcal{K}_D$  are the two radial kernels introduced in Eq. (3.23) of Rotti & Huffenberger (2019) (under the notation  ${}_I f$  and  ${}_D f$ ).

It can be convenient to extract the purely geometric kernels that multiply  $\underline{P}_q$  and  $\underline{P}_q^*$ :

$$\underline{\mathcal{K}}_{E,pq}^{(+)} \equiv \Delta\Omega \mathcal{K}_I(\beta_{qp}) e^{-2i(\alpha_{qp} + \gamma_{qp})}, \quad (\text{B3})$$

$$\underline{\mathcal{K}}_{E,pq}^{(-)} \equiv \Delta\Omega \mathcal{K}_D(\beta_{qp}) e^{2i(\alpha_{qp} - \gamma_{qp})}, \quad (\text{B4})$$

$$\underline{\mathcal{K}}_{B,pq}^{(+)} \equiv \Delta\Omega \mathcal{K}_I(\beta_{qp}) e^{-2i(\alpha_{qp} + \gamma_{qp})}, \quad (\text{B5})$$

$$\underline{\mathcal{K}}_{B,pq}^{(-)} \equiv -\Delta\Omega \mathcal{K}_D(\beta_{qp}) e^{2i(\alpha_{qp} - \gamma_{qp})}. \quad (\text{B6})$$

Equations B1 and B2 then become

$$\underline{P}_{E,p} = \sum_q \left[ \underline{\mathcal{K}}_{E,pq}^{(+)} \underline{P}_q + \underline{\mathcal{K}}_{E,pq}^{(-)} \underline{P}_q^* \right], \quad (\text{B7})$$

$$\underline{P}_{B,p} = \sum_q \left[ \underline{\mathcal{K}}_{B,pq}^{(+)} \underline{P}_q + \underline{\mathcal{K}}_{B,pq}^{(-)} \underline{P}_q^* \right]. \quad (\text{B8})$$

These expressions make explicit that the  $E/B$  projectors are linear

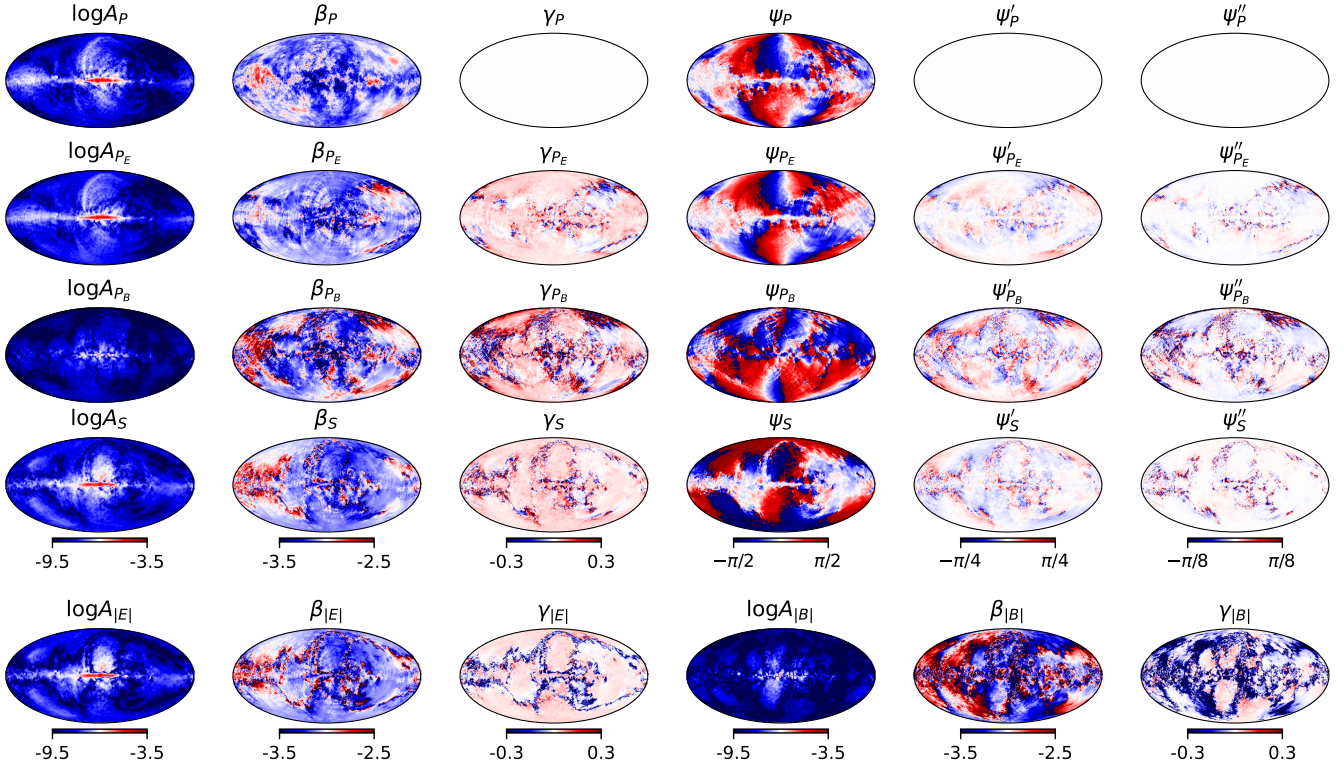
in  $(Q, U)$  (equivalently in  $\underline{P}$  and  $\underline{P}^*$ ) with geometry-only kernels  $\underline{\mathcal{K}}_{E/B,pq}^{(\pm)}$ .

Fig. 14 illustrates the action of the real-space  $E/B$  convolution kernels on a simple test case consisting of a two-dimensional positive Gaussian feature in  $Q$ . The first set of panels shows the input polarization fields  $(Q, U, P)$ , where the Gaussian structure in  $Q$  produces a localized polarization pattern with a well-defined orientation. Applying the convolution kernels yields the  $E$ -family maps  $(Q_E, U_E, P_E, E)$  and the  $B$ -family maps  $(Q_B, U_B, P_B, B)$  shown on the right (here, in practice, we did the transformation going in harmonic space).

Although the Gaussian is localized, the resulting  $E$ - and  $B$ -family fields extend over a larger area due to the non-fully-local nature of the convolution. The figure illustrates that  $P_E$  and  $P_B$  are approximately rotation- and translation-invariant representations of the polarization morphology, highlighting how even a simple structure is redistributed across neighbouring pixels.

## APPENDIX C: VERIFICATION OF RELATIONS ON TOY MODEL

In this Appendix, we explicitly verify the relations derived in Sec. 3 and used throughout Sec. 4. For the eight–component toy model described in Sec. 4, we first compute the complex spectral moments  $\underline{w}_0$ ,  $\underline{w}_1$  and  $\underline{w}_2$  of the total polarization field  $\underline{P}$  using the analytic combination rules of Eqs. 32–34, and convert them to complex log–Taylor parameters  $(\underline{A}, \underline{\beta}, \underline{\gamma})$  with Eq. 17. This yields the *predicted* maps of amplitude, spectral index, curvature and angle derivatives. Independently, we generate three closely spaced frequency maps at



**Figure 16.** Similar to Fig. 7 but for PySM  $s_5$  around 10 GHz. On the lower row, we also show the log-Taylor spectral parameters one would obtain by fitting the absolute value of  $E$  or  $B$  scalar fields.

$\nu_a = 9.999$  GHz,  $\nu_b = \nu_0 = 10$  GHz and  $\nu_c = 10.001$  GHz, and fit in each pixel a second-order complex log-Taylor expansion of  $\underline{P}_\nu$  in  $s$  (cf. Eq. 10). From these fits we obtain an *actual* set of complex log-Taylor parameters and, by inverting Eq. 17, an actual set of moments.

Fig. 15 compares these two constructions. The first two rows show, for the total polarization field  $P$ , the predicted and actual maps of  $\log A_P$ ,  $\beta_P$ ,  $\gamma_P$ , the polarization angle  $\psi_P$  and its first two derivatives with respect to  $s$ . The last two rows show the corresponding moduli and phases of the moments, displayed as  $|w_0|$ ,  $|w_1/w_0|$ ,  $|w_2/w_0|$  and the half-phases  $\frac{1}{2} \arg(w_0)$ ,  $\frac{1}{2} \arg(w_1/w_0)$ ,  $\frac{1}{2} \arg(w_2/w_0)$ . The near-identity of the predicted and actual maps for all these quantities confirms that the line-of-sight combination rules and the log-Taylor/moment relations provide an accurate description of the toy model's spectral behaviour at the pivot frequency.

#### APPENDIX D: MAPS OF THE S5 LOG-TAYLOR PARAMETERS

Figure 16 presents the full-sky maps of the complex log-Taylor spectral parameters for the PySM  $s_5$  synchrotron model around a reference frequency of 10 GHz, in direct analogy with Fig. 7 for the toy model. For each field, we show the logarithmic amplitude  $\log A$ , the spectral index  $\beta$ , the curvature parameter  $\gamma$ , and the successive orders of the polarization-angle expansion  $\psi$ ,  $\psi'$ , and  $\psi''$ .

While, as expected from the rigid-angle power-law in total polarization, there is no curvature or rotation of the polarization angle with frequency in the model, spatial variations of the spectral index in  $P$  are clearly visible, and lead to emerging curvature,  $\psi'$ , and

$\psi''$  in  $E/B$ -separated fields, because of the mechanism explained in Sec. 3.3. This spectral complexity only arises from this mechanism, as there is no intrinsic curvature or realistic physical effects such as Faraday rotation or synchrotron ageing in the model.

The scalar field  $\underline{S}$  displays a comparable level of spectral complexity as  $\underline{P}_E$  and  $\underline{P}_B$ , with large-amplitude fluctuations in both  $\beta_S$  and  $\gamma_S$  and strong angular evolution. The spin-2  $E/B$  separation redistributes spectral complexity between the two parity families:  $\underline{P}_E$  typically shows more coherent large-scale spectral patterns, while  $\underline{P}_B$  exhibits stronger small-scale fluctuations in the curvature and angle-derivative maps. Finally, the lower row illustrates that the absolute values of the scalar fields  $E$  or  $B$  individually exhibit the highest level of spectral complexity, with large-amplitude fluctuations in both  $\beta$  and  $\gamma$ .

A more quantitative comparison of the different fields, based on the statistical distributions of these spectral parameters, is presented in Sec. 4.2.2.

This paper has been typeset from a  $\text{\TeX}/\text{\LaTeX}$  file prepared by the author.